

Gemini NIFS survey of feeding and feedback processes in nearby Active Galaxies: I - Stellar kinematics

Rogemar A. Riffel^{1*}, Thaisa Storchi-Bergmann², Rogerio Riffel², Luis G. Dahmer-Hahn², Marlon R. Diniz¹, Astor J. Schönell², Natacha Z. Dametto²

¹ Departamento de Física, Centro de Ciências Naturais e Exatas, Universidade Federal de Santa Maria, 97105-900, Santa Maria, RS, Brazil

² Departamento de Astronomia, Instituto de Física, Universidade Federal do Rio Grande do Sul, CP 15051, 91501-970, Porto Alegre, RS, Brazil

Accepted 1988 December 15. Received 1988 December 14; in original form 1988 October 11

ABSTRACT

We use the Gemini Near-Infrared Integral Field Spectrograph (NIFS) to map the stellar kinematics of the inner few hundred parsecs of a sample of 16 nearby Seyfert galaxies, at a spatial resolution of tens of parsecs and spectral resolution of 40 km s^{-1} . We find that the line-of-sight (LOS) velocity fields for most galaxies are well reproduced by rotating disk models. The kinematic position angle (PA) derived for the LOS velocity field is consistent with the large scale photometric PA. The residual velocities are correlated with the hard X-ray luminosity, suggesting that more luminous AGN have a larger impact in the surrounding stellar dynamics. The central velocity dispersion values are usually higher than the rotation velocity amplitude, what we attribute to the strong contribution of bulge kinematics in these inner regions. For 50% of the galaxies, we find an inverse correlation between the velocities and the h_3 Gauss-Hermite moment, implying red wings in the blueshifted side and blue wings in the redshifted side of the velocity field, attributed to the movement of the bulge stars lagging the rotation. Two of the 16 galaxies (NGC 5899 and Mrk 1066) show an S-shape zero velocity line, attributed to the gravitational potential of a nuclear bar. Velocity dispersion (σ) maps show rings of low- σ values ($\sim 50 - 80 \text{ km s}^{-1}$) for 4 objects and “patches” of low- σ for 6 galaxies at 150–250 pc from the nucleus, attributed to young/ intermediate age stellar populations.

Key words: galaxies: kinematics and dynamics – galaxies: active – galaxies: ISM – infrared: galaxies

1 INTRODUCTION

Active Galactic Nuclei (AGN) characterize a critical phase in galaxy evolution in which its nuclear super-massive black hole (SMBH) is being fed due to gas accretion to the nuclear region. Once the accretion disk surrounding the SMBH is formed, feedback processes begin to occur, comprising jets of relativistic particles emitted from the inner rim of the accretion disk, winds emanating from outer regions of the disk and radiation emitted by the hot gas in the disk or by its corona (Frank, King & Raine. 2002; Elvis 2000; Ciotti et al. 2010). The AGN feeding and feedback processes couple the growth of the SMBHs and their host galaxies, and are claimed to explain the correlation between the mass of the SMBH and the mass of the galaxy bulge (Ferrarese & Ford 2005; Somerville et al. 2008; Kormendy & Ho 2013). The feeding processes are a necessary condition to trigger the nuclear activity,

while the feedback processes are now a fundamental ingredient in galaxy evolution models: without AGN feedback, the models cannot reproduce the properties of the massive galaxies – these galaxies end up forming too many stars (Springel et al. 2005; Fabian 2012; Terrazas et al. 2016).

The study of feeding and feedback processes in AGNs requires a detailed mapping of the gas and stellar kinematics in the vicinity of the central engine. Usually these studies are based on high spatial resolution Integral Field Spectroscopy (IFS, e.g. Fathi et al. 2006; Barbosa et al. 2009, 2014; Sánchez et al. 2009; Hicks et al. 2009, 2013; Storchi-Bergmann et al. 2007, 2009, 2010; Mazzalay et al. 2014; Riffel et al. 2013; Riffel & Storchi-Bergmann 2011a; Riffel, Storchi-Bergmann & Riffel 2014; Diniz et al. 2015). To isolate and quantify gas streaming motions towards the center of galaxies or gas outflows from the nucleus through the gas kinematics, it is necessary to properly map the motions of the gas due to the gravitational potential of the galaxy. A way to map the gravitational potential of the galaxies is by two-dimensional

* E-mail: rogemar@ufsm.br

Table 1. Sample: (1) Galaxy’s name; (2) redshift; (3) nuclear activity; (4) Hubble type as quoted in NED; (5) Spectral Resolution in Å; (6) Angular Resolution; (7) Spectral Band; (8) Gemini project code; (9) total exposure time; (10) hard X-ray luminosity (14-195 keV) from the Swift-BAT 60-month catalogue (Ajello et al. 2012); (11) reference for the stellar kinematics.

1	2	3	4	5	6	7	8	9	10	11
Galaxy	z	Act.	Hub. Type	Sp. R.	An. R.	B	Project ID	Exp. T.	$\log L_X$ [erg s ⁻¹]	Ref.
NGC788	0.014	Sy2	SA0/a?(s)	3.5	0'13	K	GN-2015B-Q-29	4400	43.2	a
NGC1052†	0.005	Sy2	E4	3.4	0'14	KI	GN-2010B-Q-25	2400	41.9	a
NGC2110	0.008	Sy2	SAB0 ⁻	3.4	0'15	KI	GN-2010B-Q-25	3600	43.3	b
NGC3227	0.004	Sy1.5	SAB(s)a pec	3.4	0'13	KI	GN-2016A-Q-6	2400	42.3	a
NGC3516	0.009	Sy1.5	(R)SB0 ⁰ ?(s)	3.6	0'15	K	GN-2015A-Q-3	4500	42.7	a
NGC4051†	0.002	Sy1	SAB(rs)bc	3.2	0'17	K	GN-2006A-SV-123	4500	41.5	c
NGC4235	0.008	Sy1	SA(s)a edge-on	3.4	0'13	KI	GN-2016A-Q-6	4000	42.3	a
NGC4388	0.008	Sy2	SA(s)b? edge-on	3.5	0'14	K	GN-2015A-Q-3	800	43.3	a
NGC5506	0.006	Sy1.9	Sa pec edge-on	3.5	0'15	K	GN-2015A-Q-3	4000	43.1	a
NGC5548†	0.017	Sy1	(R')SA0/a(s)	3.5	0'20	KI	GN-2012A-Q-57	2700	43.4	a
NGC5899†	0.009	Sy2	SAB(rs)c	3.5	0'12	KI	GN-2013A-Q-48	4600	42.1	a
NGC5929†	0.008	Sy2	Sab? pec	3.2	0'12	KI	GN-2011A-Q-43	6000	—	d
Mrk607†	0.009	Sy2	Sa? edge-on	3.5	0'12	KI	GN-2012B-Q-45	6000	—	a
Mrk766	0.013	Sy1.5	(R')SB(s)a?	3.5	0'19	KI	GN-2010A-Q-42	3300	42.8	a
Mrk1066†	0.012	Sy2	(R)SB0 ⁺ (s)	3.3	0'15	KI	GN-2008B-Q-30	4800	—	e
Mrk1157†	0.015	Sy2	(R')SB0/a	3.5	0'12	KI	GN-2009B-Q-27	3300	—	f

†These galaxies do not follow all selection criteria and are part of the complementary sample.

a – This work; b – Diniz et al. (2015); c – Riffel et al. (2008); d – Riffel et al. (2015a); e – Riffel & Storchi-Bergmann (2011a);

f – Riffel & Storchi-Bergmann (2011b)

mapping of the stellar kinematics. So far, studies available for nearby galaxies show that the stellar kinematics usually present regular rotation within the inner kiloparsec (e.g. Barbosa et al. 2006; Ganda et al. 2006) and thus can be used to isolate possible non-circular motions from the gas kinematics (e.g. Riffel et al. 2008; Riffel & Storchi-Bergmann 2011a; Diniz et al. 2015).

Adaptive optics IFS at 10-m class telescopes provides an unprecedented possibility to map the stellar kinematics of nearby galaxies at spatial resolutions of a few tens of parsecs. So far, adaptive optics systems are available mainly in near-infrared (near-IR) wavelengths, where the dust extinction at the central regions of galaxies is less important than at optical bands. In addition, strong absorption CO bands are present in the spectra of galaxies, originated in giant and super-giant stars that dominate the continuum emission in the central regions (e.g. Maraston 2005; Riffel et al. 2015c). Thus, near-IR IFS at 10-m telescopes provides a unique tool to map the stellar kinematics at central region of active galaxies, at unprecedented spatial resolution, by fitting the CO absorption band-heads (e.g. Riffel et al. 2015b).

In this paper, we map the stellar kinematics of the inner 3''×3'' of a sample of 16 nearby Seyfert galaxies. This work is part of a larger project in which our group AGNIFS (*AGN Integral Field Spectroscopy*) aims to study the feeding and feedback processes of a sample of 30 nearby Seyfert galaxies, selected by their X-ray luminosity. The kinematic maps presented here will be used to isolate gas non-circular motions in future works by our group and to quantify gas inflows and outflows.

This paper is organized as follows: section 2 presents the sample and a description of the observations and data reduction procedure, while the spectral fitting procedure is presented in sec. 3. The resulting stellar kinematics maps are presented and discussed in section 4 and the kinematic derived parameters are compared with those characterizing the large scale disks of the host galaxies in section 5.1. Finally, section 6 presents the main conclusions of this work.

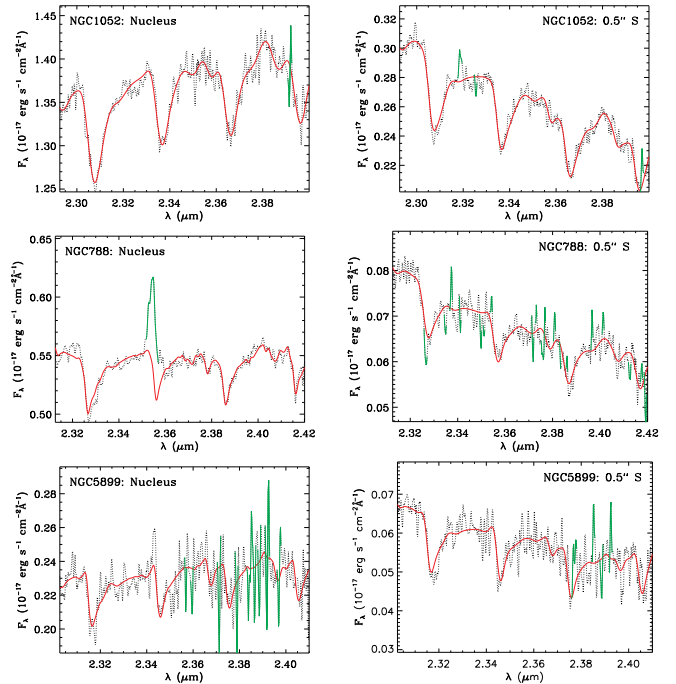


Figure 1. Examples of fits for the nuclear spectrum (left) and typical extra nuclear spectrum (right) for NGC 1052 (top panels), NGC 788 (center panels) and NGC 5899 (bottom panels). The observed spectra are shown as black dotted lines, the best fitted models as red continuous lines and the masked regions (following the criteria explained in the text) during the fits are shown in green.

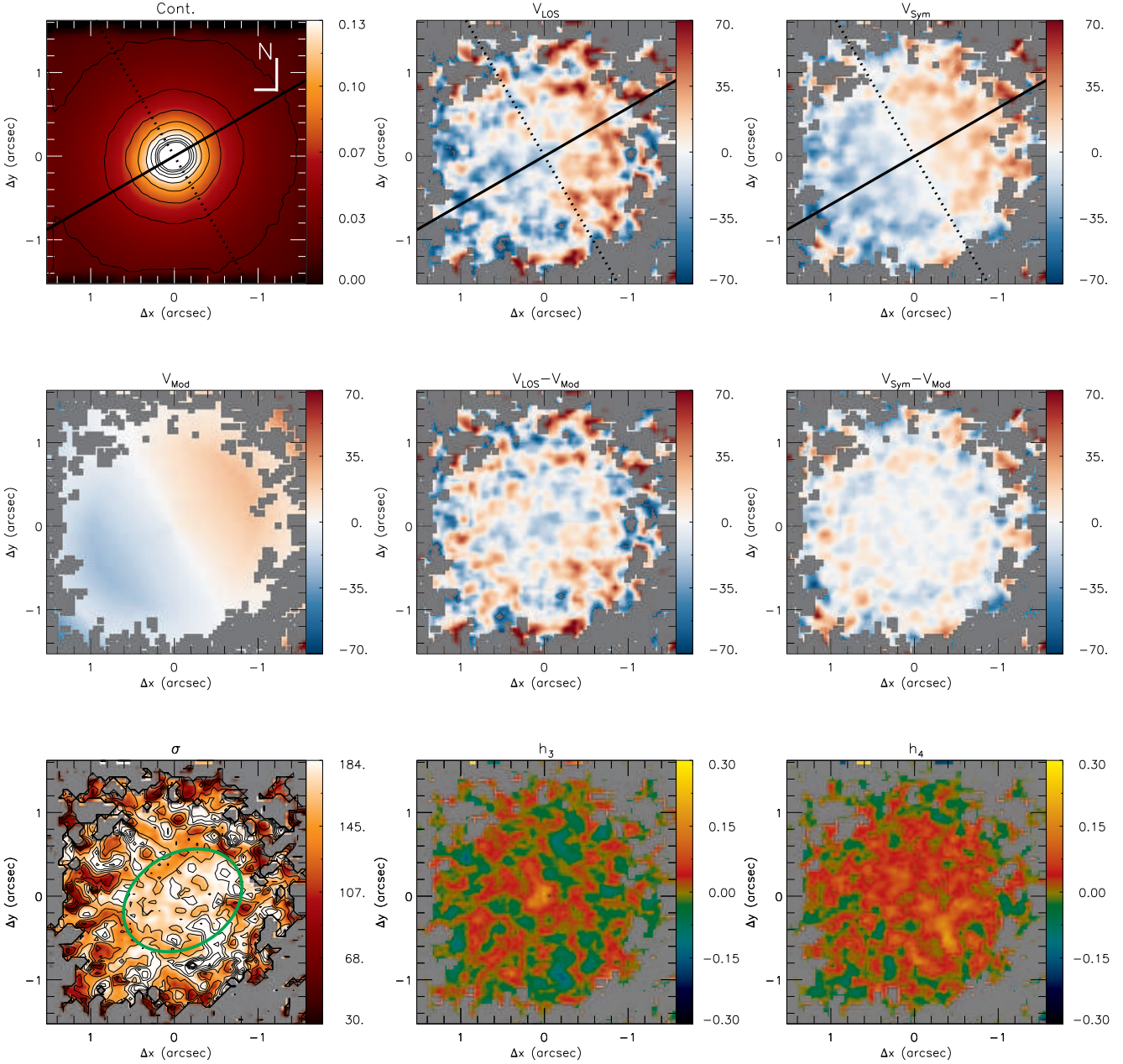


Figure 2. NGC 788: Top-left: K-band continuum image obtained by averaging the spectra, with the color bar shown in units of $10^{-17} \text{ erg s}^{-1} \text{ cm}^{-2} \text{ \AA}^{-1}$; top-middle: stellar velocity field; top-right: symmetrized velocity field; middle-left: rotating disk model; middle-middle: residual map for the symmetrized velocity field; middle-right: residual map for the observed velocity field; bottom-left: stellar velocity dispersion; bottom-middle: h_3 Gauss-Hermite moment and bottom-right: h_4 Gauss-Hermite moment. Gray regions are masked locations and correspond to regions where the signal-to-noise of the spectra was not high enough to get reliable fits. The continuous line identifies the orientation of the line of nodes and the dotted line marks the orientation of the minor axis of the galaxy. North is up and East left in all maps. The color bar for velocity, model, residual maps and σ show the velocities in units of km s^{-1} and the systemic velocity of the galaxy was subtracted from the observed velocities.

2 SAMPLE AND OBSERVATIONS

2.1 The sample

Our sample comprises 16 AGN host galaxies: 8 from a large Gemini proposal (PI Storchi-Bergmann) to obtain NIFS (Near-Infrared Integral Field Spectrograph) observations of 20 AGN selected from the Swift-BAT 60-month catalogue (Ajello et al. 2012) to have 14–

195 keV luminosities $L_X \geq 10^{41.5} \text{ erg s}^{-1}$, and 8 from previous similar NIFS observations by our group of nearby AGN hosts. Four of these 8 galaxies have similar L_X luminosities and 4 are not in the Swift-BAT catalog. One additional source (Mrk 79) was observed in previous run with similar NIFS configuration, but the signal-to-noise ratio of the CO absorption bandheads was not high enough to allow stellar kinematics measurements. By the end of 2018, we

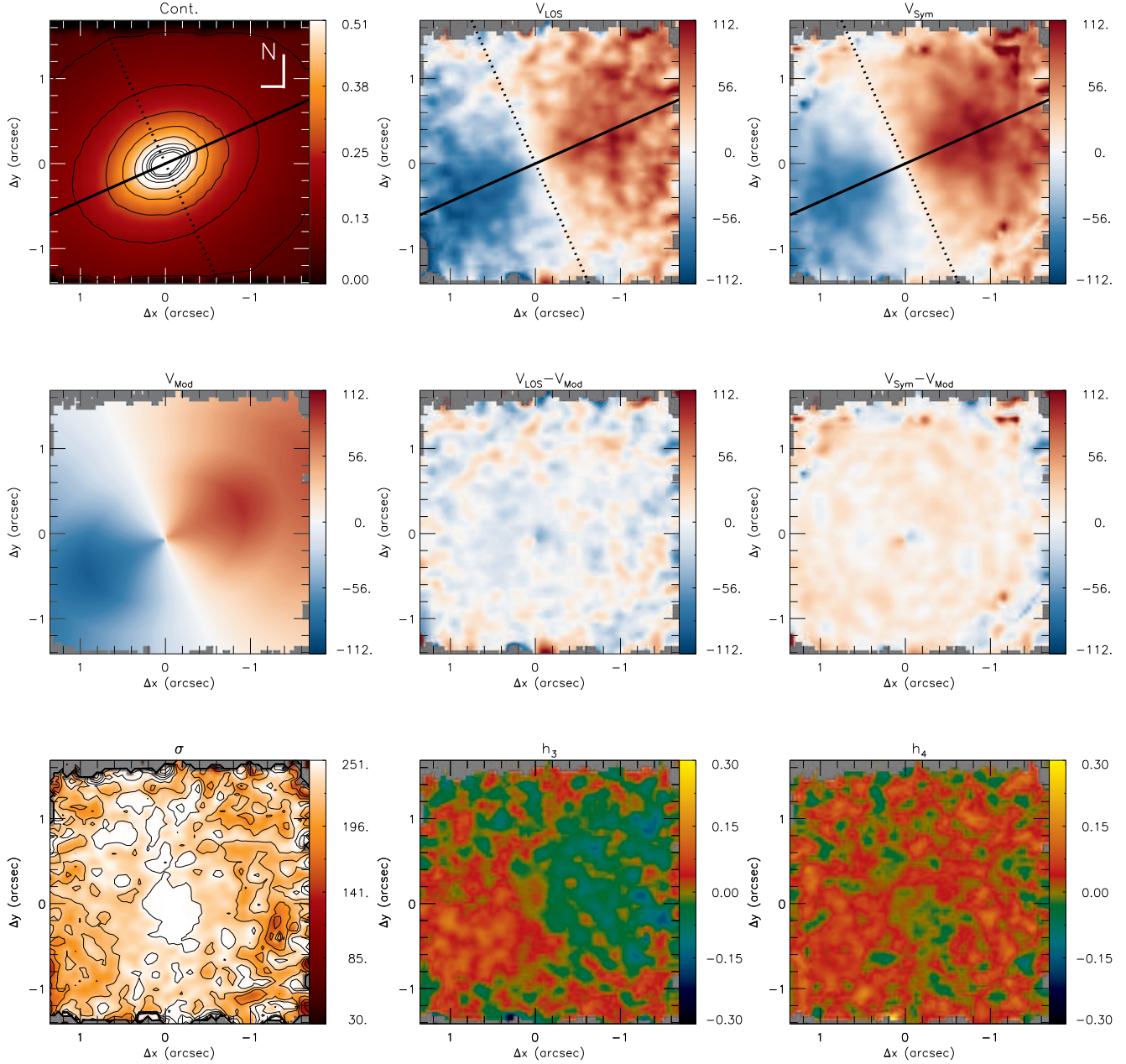


Figure 3. Same as Fig. 2 for NGC 1052.

should have additional observations of another 13 galaxies of the large proposal and thus will have in the end a total of 29 galaxies comprising 20 Swift-BAT selected galaxies plus the 8 galaxies included in the present study (plus Mrk 79) that comprise what we call a “complementary sample”, and identified by the symbol \dagger in Table 1.

Additional criteria for the sample is that the redshift is $z \leq 0.015$, and to be accessible for NIFS ($-30^\circ < \delta < 73^\circ$). The L_X criterium above defining the sample of the large proposal was adopted because the the Swift-BAT 14–195 keV band measures direct emission from the AGN rather than scattered or re-processed emission, and is much less sensitive to obscuration in the line-of-sight than soft X-ray or optical wavelengths, allowing a selection

based only on the AGN properties. In order to assure that we would be able to probe the feeding and feedback processes via the gas kinematics we further selected the galaxies having previously observed extended gas emission (e.g. Schmitt & Kinney 2000) and $[\text{O III}]\lambda 5007$ luminosities. We have excluded from the sample a few galaxies that had guiding problems in the observations. A complete characterization of the sample will be presented in a forthcoming paper (Riffel et al., in preparation).

So far, we have already observed 20 galaxies with NIFS, but only for 16 of them we were able to measure the stellar kinematics by fitting the K-band CO absorption bands at $2.3 \mu\text{m}$. We were not able to obtain reliable fits of the remaining four objects (Mrk 3, Mrk 79, NGC 4151 and NGC 1068) due to the dilution of the K-

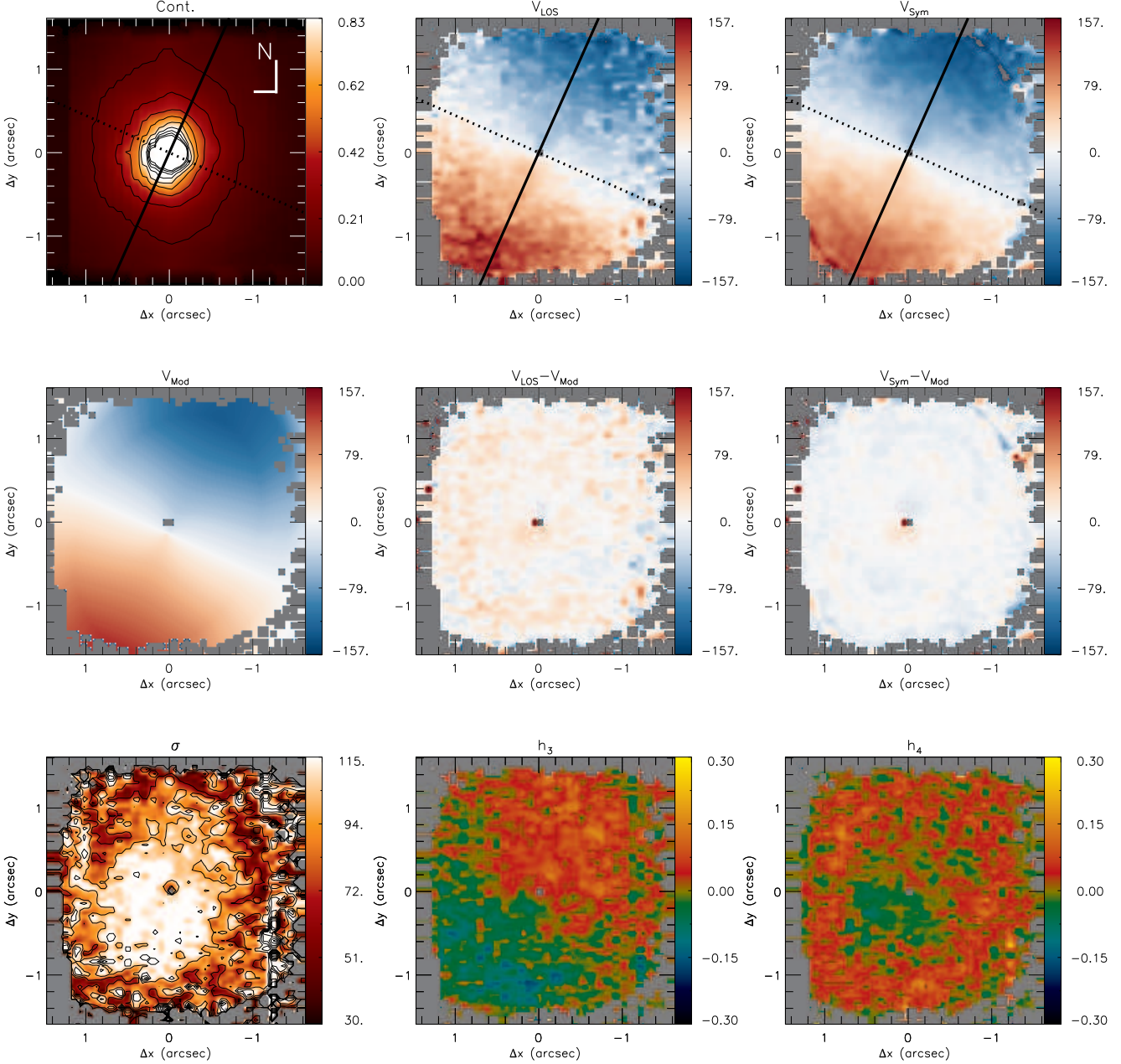


Figure 4. Same as Fig. 2 for NGC 3227.

band CO band-heads due to strong continuum emission. For the latter two, the stellar kinematics has already been studied using the H-band spectra (Onken et al. 2014; Storchi-Bergmann et al. 2012). The 16 galaxies selected for the present study are listed in Table 1, together with relevant information.

2.2 Observations

We used the Gemini Near-Infrared Integral Field Spectrograph (NIFS, McGregor et al. 2003) to observe the galaxies listed in Table 1. All observations were obtained using the Gemini North Adaptive Optics system ALTAIR from 2008 to 2016. The observations followed the standard Object-Sky-Sky-Object dither se-

quence, with off-source sky positions since all targets are extended, and individual exposure times that varied according to the target. The “HK_G0603” filter and the “KL_G5607” and “K_G5605” gratings were used during the observations. Most of the observations were performed in the K_f band, with the spectra centred at $2.3 \mu\text{m}$, while for five galaxies the spectra were obtained at the K band and centred at $2.2 \mu\text{m}$. The spectral range for the K_f data is $\sim 2.080 - 2.500 \mu\text{m}$ and for the K band is $\sim 1.980 - 2.400 \mu\text{m}$. Both ranges include the ^{12}CO and ^{13}CO absorption band-heads at $\sim 2.3 \mu\text{m}$ for all galaxies, used to measure the stellar kinematics.

The spectral resolution ranges between 3.2 and 3.6 \AA , as obtained from the measurement of the full width at half maximum (FWHM) of ArXe lamp lines, used to wavelength calibrate the

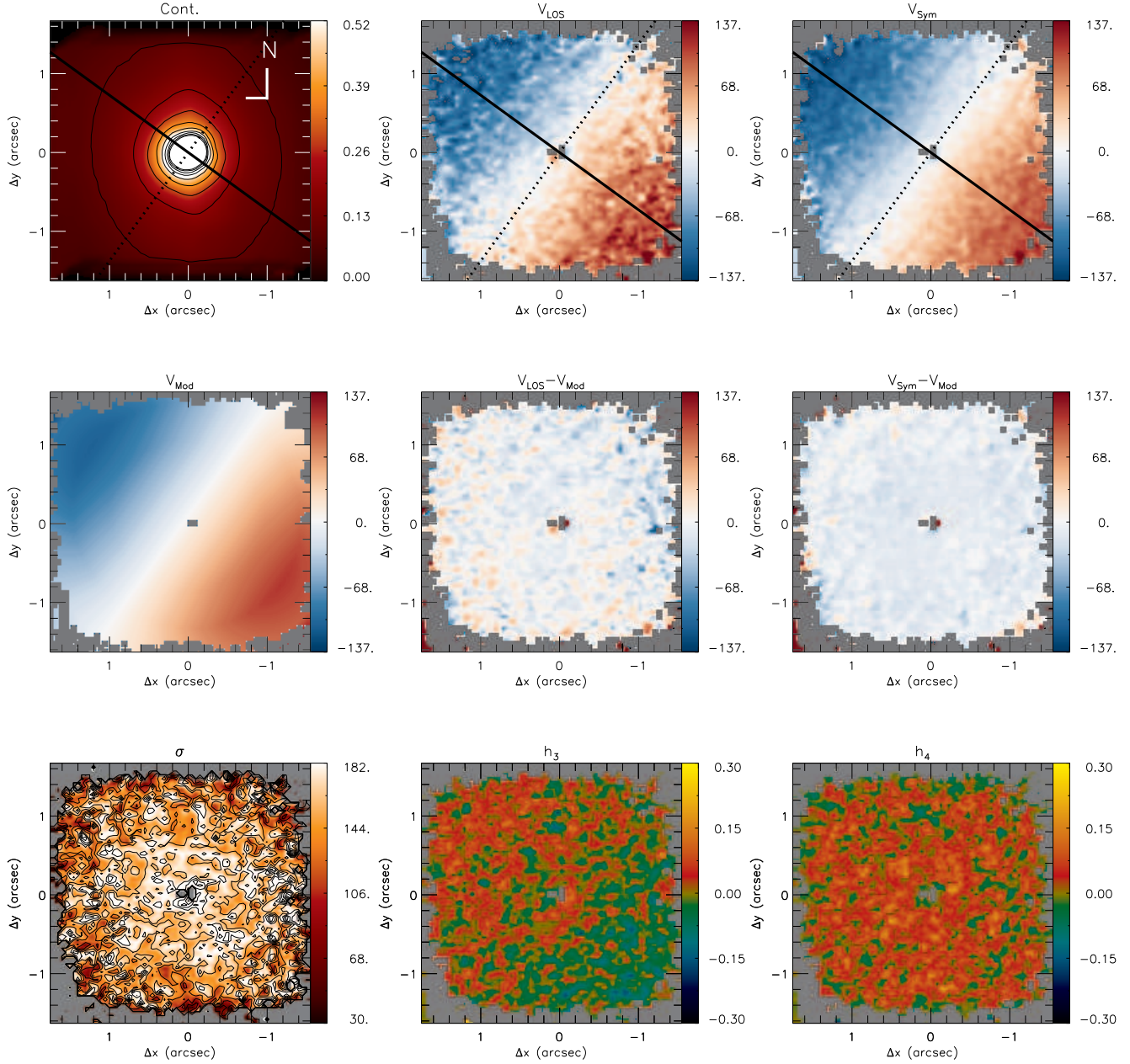


Figure 5. Same as Fig. 2 for NGC 3516.

spectra, close to the central wavelength. This translates to resolutions in the range $42\text{--}47\text{ km s}^{-1}$ in the velocity space. The angular resolution is in the range $0''.12\text{--}0''.20$, derived from the FWHM of flux distribution of the standard stars, corresponding to few tens of parsecs at the distance of most galaxies. More details about the observations are shown in Table 1.

2.3 Data reduction

The data reduction followed the standard procedure and was accomplished by using tasks specifically developed for NIFS data reduction, contained in the NIFS package, which is part of GEMINI IRAF package, as well as generic IRAF tasks and IDL scripts. The

data reduction procedure included the trimming of the images, flat-fielding, sky subtraction, wavelength and s-distortion calibrations. The telluric absorptions have been removed using observations of telluric standard stars with A spectral type. These stars were used to flux calibrate the spectra of the galaxies by interpolating a black body function to their spectra. Finally, datacubes were created for each individual exposure at an angular sampling of $0''.05 \times 0''.05$ and combined in a final datacube for each galaxy. All datacubes cover the inner $\sim 3'' \times 3''$, with exception of the datacube for NGC 4051 that covers the inner $\sim 3'' \times 4''$, via spatial dithering during the observations (Riffel et al. 2008).

The median value of the signal-to-noise ratio (S/N) in the continuum of our sample ranges from 10 to 30, with the maxi-

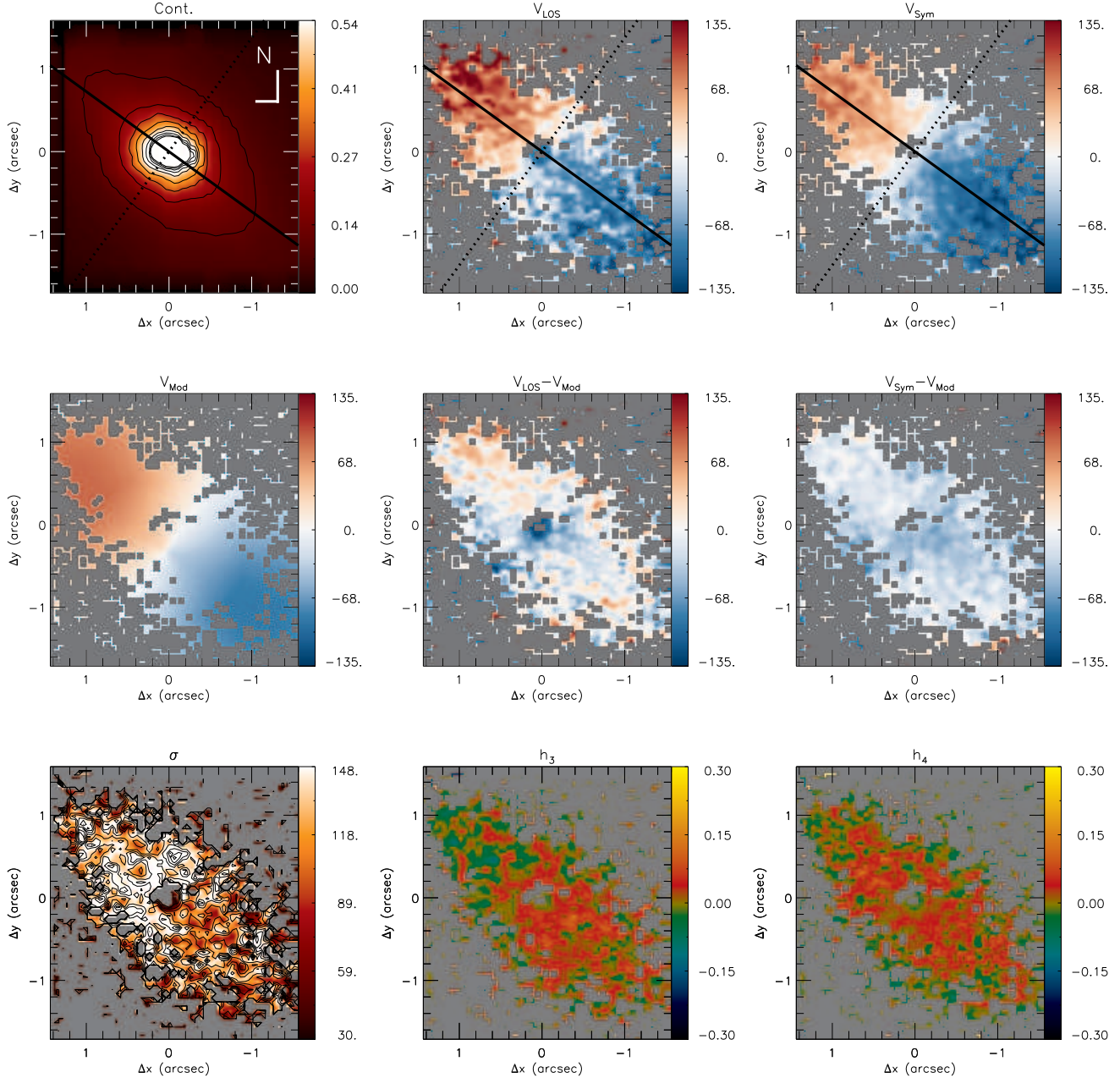


Figure 6. Same as Fig. 2 for NGC 4235.

imum value of up to $S/N \sim 100$ observed for the nuclear spectrum of NGC 4051. The median value of the S/N for the ^{12}CO (2-0) band-head at $2.29 \mu\text{m}$ is larger than 3 for all galaxies of the sample.

Detailed descriptions of the observations and data reduction procedures for the galaxies already analyzed are presented in Riffel, Storchi-Bergmann & Nagar (2010) for Mrk 1066, Riffel & Storchi-Bergmann (2011b) for Mrk 1157, Diniz et al. (2015) for NGC 2110 and Riffel et al. (2008) for NGC 4051. For the remaining objects a more detailed discussion will be presented in a forthcoming paper (Riffel et al., in preparation).

3 SPECTRAL FITTING

The stellar line-of-sight velocity distribution (LOSVD) of each galaxy was obtained by fitting the spectra within the spectral range $\sim 2.26\text{--}2.40 \mu\text{m}$ (rest wavelengths), which includes the CO absorption band-heads from ~ 2.29 to $\sim 2.40 \mu\text{m}$ (Winge, Riffel & Storchi-Bergmann 2009), usually among of the strongest absorption lines in the central region of galaxies (e.g. Riffel, Rodríguez-Ardila & Pastoriza 2006; Riffel et al. 2015c). The used spectral range also includes weaker absorption lines from Mg I and Ca I at $2.26\text{--}2.28 \mu\text{m}$. The spectra were fitted by using the penalized Pixel-Fitting `PPXF` method (Cappellari & Emsellem 2004), that finds the best fit to a galaxy spectrum by convolving

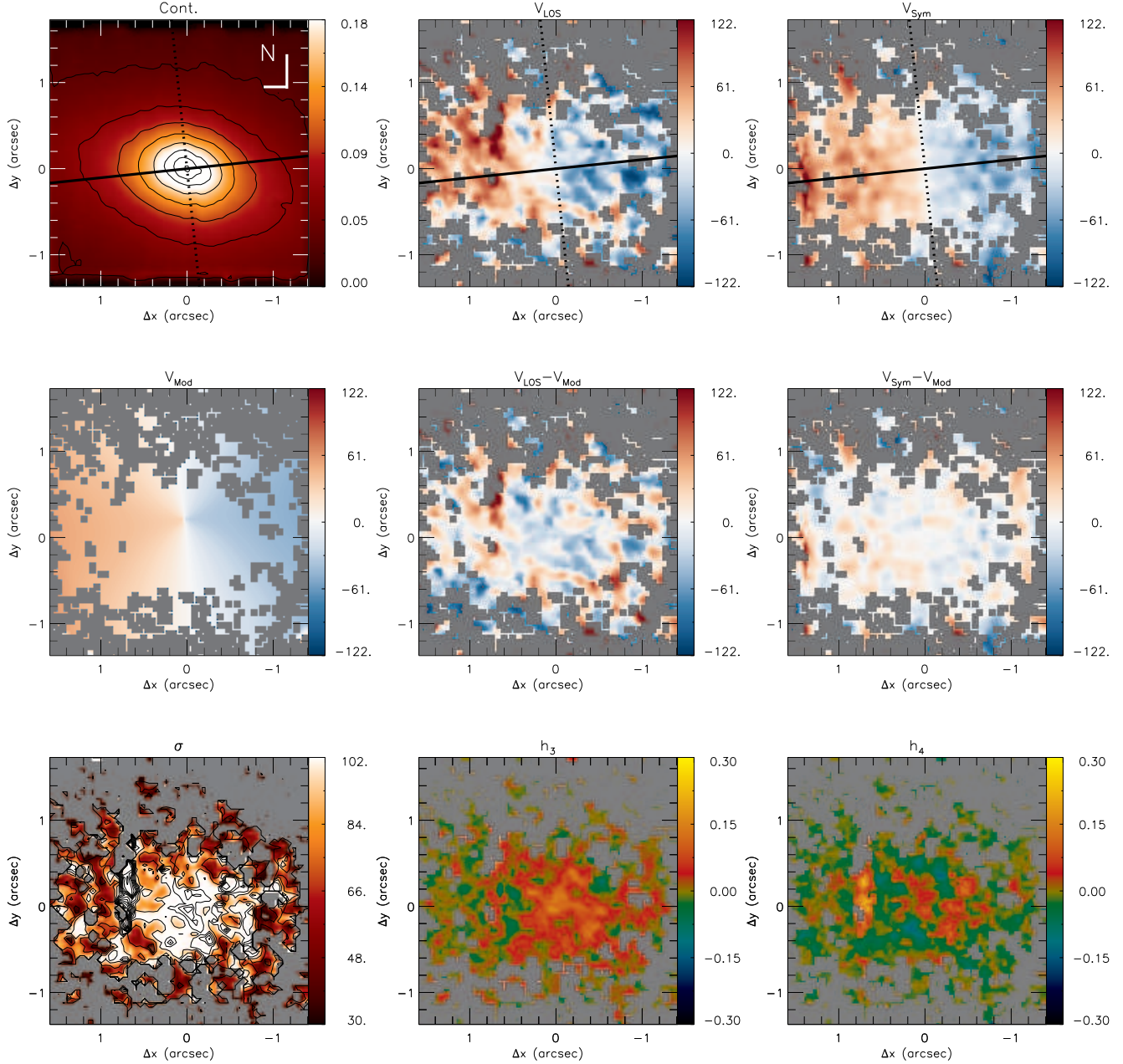


Figure 7. Same as Fig. 2 for NGC 4388.

stellar spectra templates with a given LOSVD, under the assumption that it is reproduced by Gauss-Hermite series.

The *PPXF* code requires the use of spectral templates that are used to reproduce the galaxy’s spectrum. We used the spectra of the Gemini library of late spectral type stars observed with the Gemini Near-Infrared Spectrograph (GNIRS) IFU and NIFS (Winge, Riffel & Storchi-Bergmann 2009) as stellar templates. The spectral resolution of the stellar library is very similar to that of the spectra of the galaxies of our sample and the library includes stars with spectral types from F7 to M5, minimizing the template mismatch problem.

The spectral range used in the fit includes the $[\text{Ca VIII}]\lambda 2.321\ \mu\text{m}$ emission line, which “contaminates” the

$(3-1)^{12}\text{CO}$ bandhead and affects the stellar kinematics measurements (Davies et al. 2006; Riffel et al. 2008). The $[\text{Ca VIII}]$ is seen at the nucleus and close vicinity, being unresolved for most galaxies of our sample and we have excluded its spectral region from the fit when the line is present. In addition, we used the *clean* parameter of *PPXF* to reject all spectral pixels deviating more than 3σ from the best fit, in order to exclude possible remaining sky lines and spurious features.

In Figure 1 we present examples of typical fits for the galaxies NGC 1052, NGC 788 and NGC 5899. The left panels show the fits for the nuclear spectrum, while extra-nuclear spectra are shown at the right panels, extracted at $0''.5$ south of the nucleus – chosen to represent typical extra-nuclear spectra. The observed

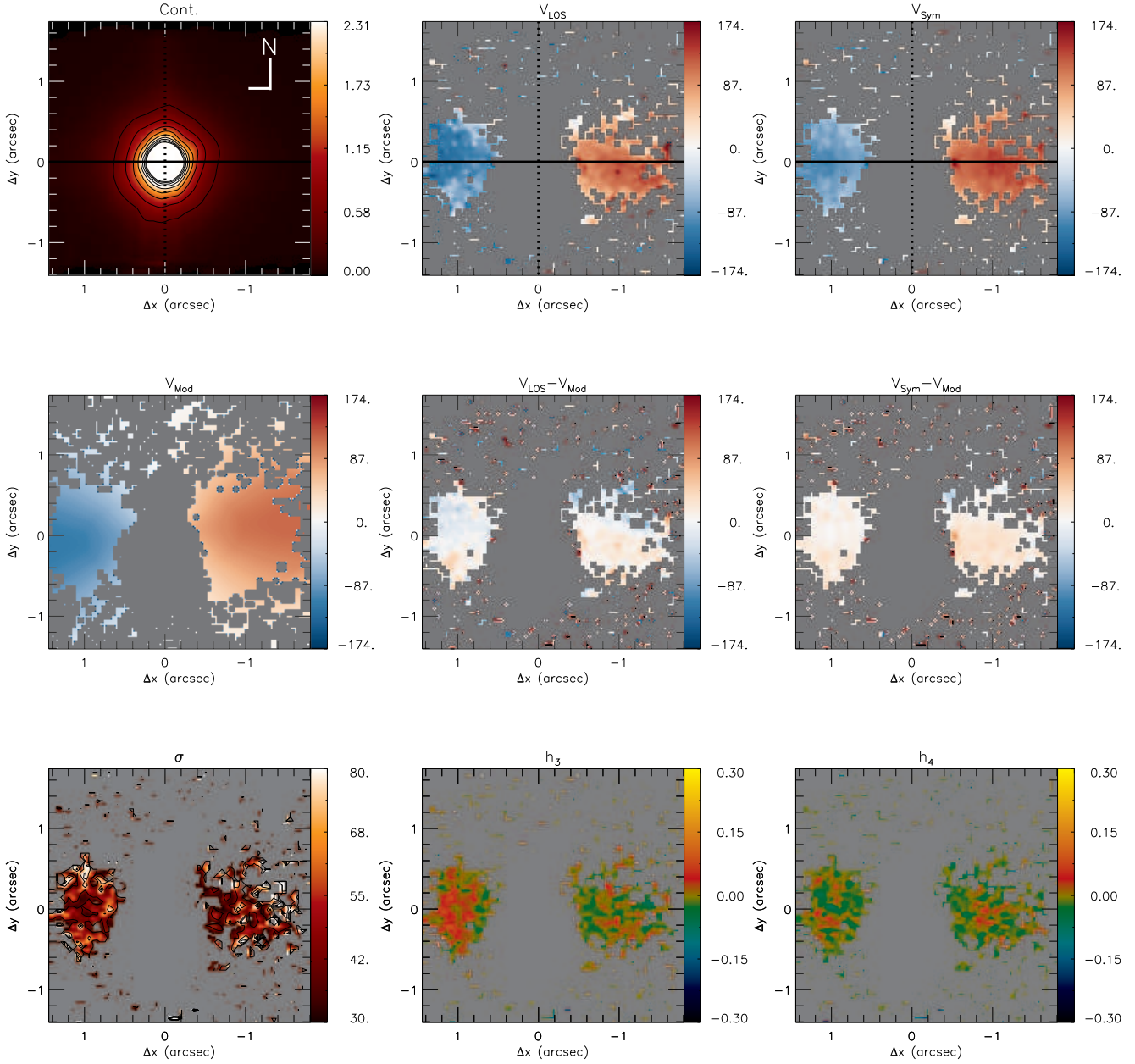


Figure 8. Same as Fig. 2 for NGC 5506.

spectra are shown as black dotted lines, the fits are shown in red and the regions masked during the fits, following the criteria explained above, are shown in green. As can be seen for NGC 788, the cleaning procedure properly excluded the region affected by the $[\text{Ca VII}]\lambda 2.321\ \mu\text{m}$ emission line, as well as spurious features. For all galaxies, the standard deviations of the residuals (observed – model) are similar to that of the galaxy spectra derived within a $200\ \text{\AA}$ spectral window, blue-ward to the first CO absorption band-head, meaning that the spectra are well reproduced by the models.

The `PPXF` code returns as output, measurements for the radial velocity (V_{LOS}), stellar velocity dispersion (σ), and higher order Gauss-Hermite moments (h_3 and h_4) for each spatial position, as well as their associated uncertainties. Using the results of the fit, we

have constructed two-dimensional maps for each fitted parameter (V_{LOS} , σ , h_3 and h_4), which are presented in the next section.

4 STELLAR KINEMATICS

Figures 2–12 show the resulting maps for the stellar kinematics of our sample. The stellar kinematics for NGC 4051, NGC 2110, NGC 5929, Mrk 1066 and Mrk 1157 was already discussed in previous works by our group (see references in Table 1). Thus, we present the corresponding maps for these galaxies in Figures A1–A5 of the Appendix A, to be published on-line only.

In order to characterize the LOS velocity fields, we have sym-

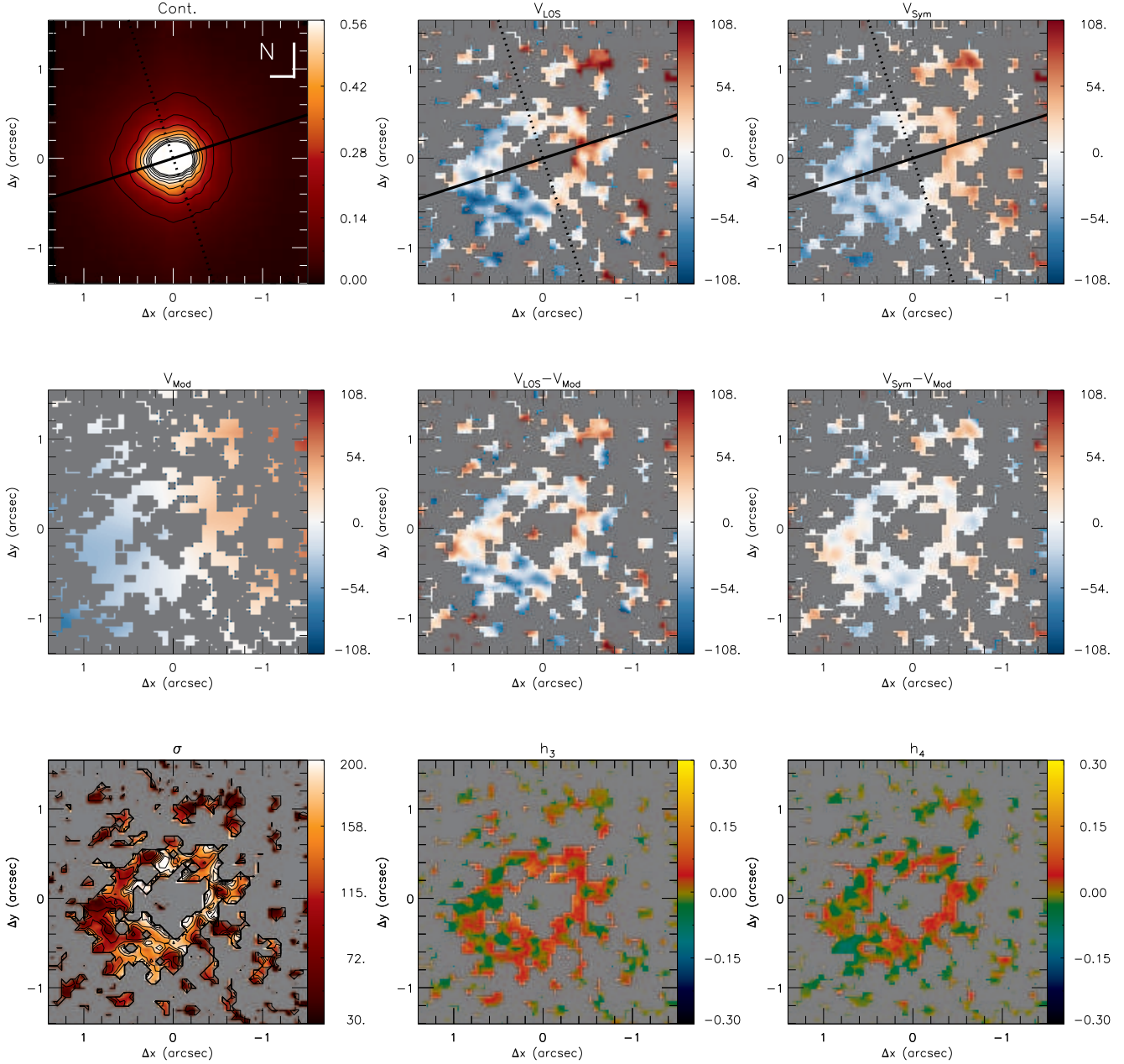


Figure 9. Same as Fig. 2 for NGC 5548.

metrized the stellar velocity field, using the *fit_kinematic_pa*¹ routine. This routine measures the global kinematic position-angle and systemic velocity of the galaxy from integral field observations of the galaxy's kinematics. The method is described in Krajnović et al. (2006). Cappellari et al. (2007) and Krajnović et al. (2011) show examples of application of the method to study the large-scale stellar kinematics of large sample of galaxies of the SAURON and ATLAS^{3D} surveys.

In addition, we fitted the LOS velocity fields by a ro-

tating disk model. The model was obtained using the DiskFit routine (Sellwood & Spekkens 2015; Sellwood & Sánchez 2010; Spekkens & Sellwood 2007; Reese et al. 2007; Barnes & Sellwood 2003; Kuzio de Naray et al. 2012) to fit the symmetrized velocity fields. This code fits non-parametric kinematic models to a given velocity field allowing the inclusion of circular and non-circular motions in a thin disk. Examples of application of this code for the gas and stellar kinematics of the inner region of active galaxies are shown in Fischer et al. (2015) and Riffel et al. (2015a), respectively. We fitted the symmetrized velocity field, instead of the observed one, as the rotating disk model is expected to be symmetric and small fluctuations in velocity due to higher uncertainties at some locations would result in a worse model for the stellar kine-

¹ This routine was developed by M. Cappellari and is available at <http://www-astro.physics.ox.ac.uk/mxc/software>

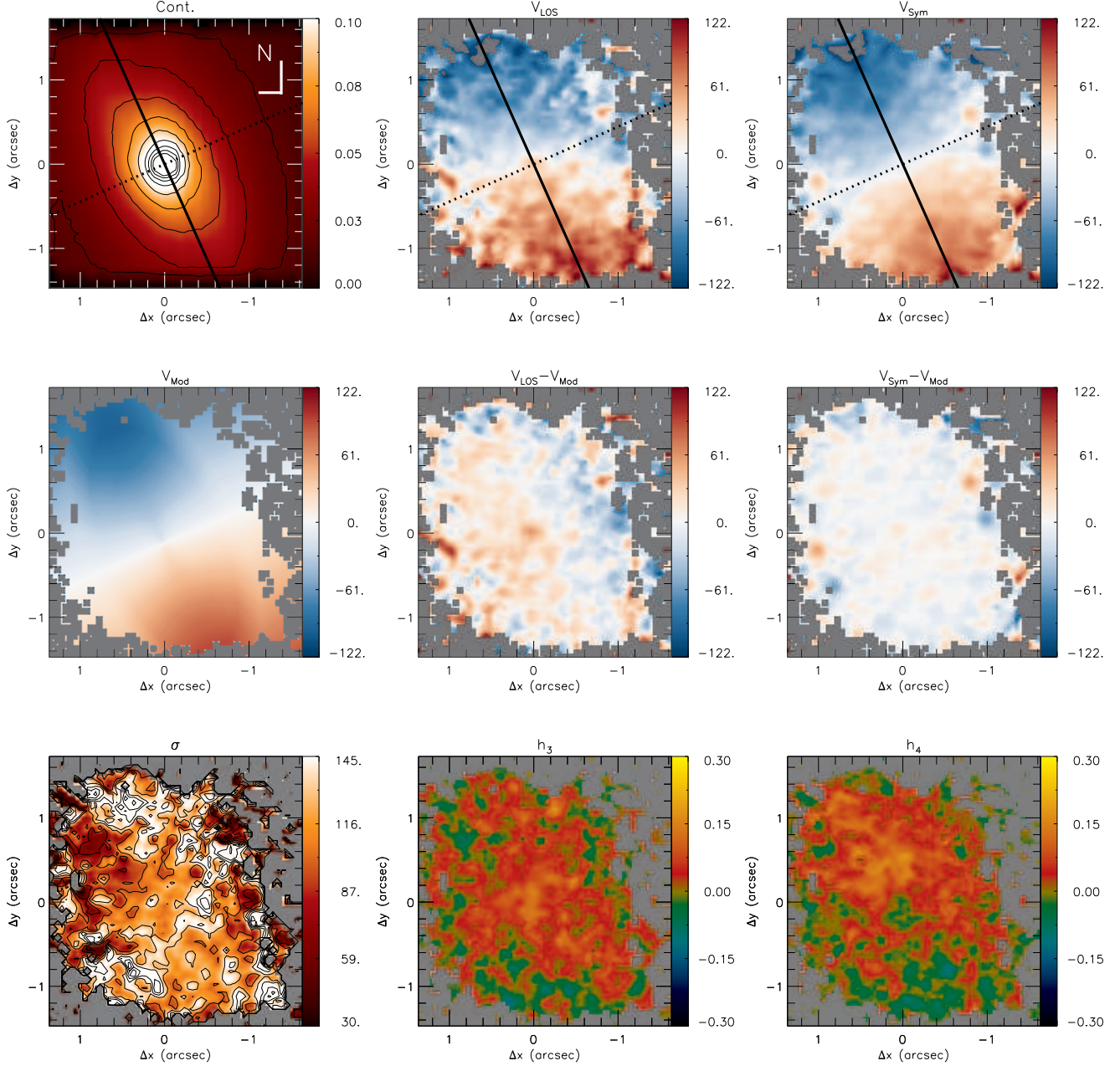


Figure 10. Same as Fig. 2 for NGC 5899.

matics. During the fit, we have fixed the kinematical center to the position of the peak of the continuum emission and the systemic velocity and orientation of the line of nodes of the galaxy were fixed as the values obtained from the symmetrization of the velocity field, in order to reduce the number of parameters to be fitted. The ellipticity and disk inclination were allowed to vary during the fit and the resulting fitted values for each galaxy are shown in Table 2.

Figures 2–12 are organized as follows:

- Top-left panel: K-band image, obtained as the average flux between 2.20 and 2.30 μm . The continuous line shows the orientation of the kinematic major axis and the dotted line shows the orientation of the minor axis of the galaxy, obtained from the symmetriza-

tion of the stellar velocity field. The color bar shows the flux scale in units of $10^{-17} \text{ erg s}^{-1} \text{ cm}^{-2} \text{ \AA}^{-1}$.

- Top-center panel: Measured LOS stellar velocity field obtained from the fit of the spectra using the `PPXF` routine (Cappellari & Emsellem 2004), following the procedure described in Section 3.

- Top-right panel: Symmetrized velocity field. The color bar is shown in units of km s^{-1} and the systemic velocity of the galaxy was subtracted.

- Middle-left panel: Rotating disk model, obtained by fitting the symmetrized velocity field.

- Middle-center panel: Residual map obtained by subtracting the rotating disk model from the observed velocity field.

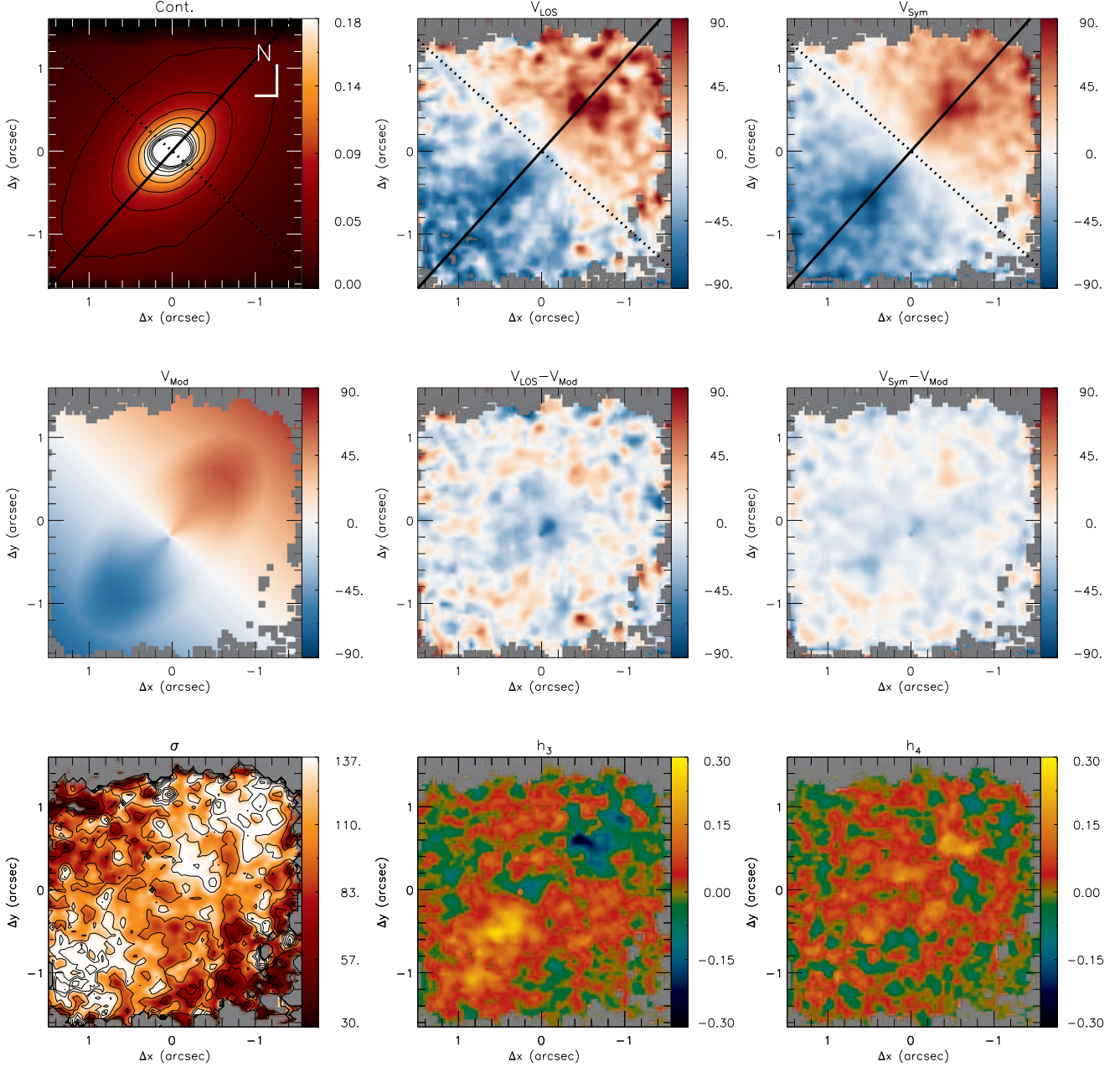


Figure 11. Same as Fig. 2 for Mrk 607.

- Middle-right panel: Residual map obtained by subtracting the rotating disk model from the symmetrized velocity field, constructed in order to verify if the velocity field is well reproduced by the model.

- Bottom-left panel: Stellar velocity dispersion (σ) map. The color bar shows the σ in km s^{-1} units.

- Bottom-center panel: map for the h_3 Gauss-Hermite moment. The h_3 moment measures asymmetric deviations of the LOSVD from a Gaussian velocity distribution (van der Marel & Franx 1993; Gerhard 1993; Riffel 2010). High (positive) h_3 values correspond to the presence of red wings in the LOSVD while low (negative) h_3 values correspond to the presence of blue wings.

- Bottom-right panel: map for the h_4 Gauss-Hermite moment,

that measures symmetric deviations of the LOSVD relative to a Gaussian velocity distribution. High (positive) h_4 values indicate LOSVD is more “pointy” than a Gaussian, while low (negative) h_4 values indicate profiles more “boxy” than a Gaussian.

In all figures, North is up and East to the left and the gray regions represent masked locations. In these regions it was not possible to obtain good fits due to low signal-to-noise ratio of the spectra or due to the non detection of absorption lines (e.g. due to the dilution of the absorption lines by strong AGN continuum emission). The masked regions correspond to locations where the uncertainty in velocity or velocity dispersion is higher than 30 km s^{-1} , while for most other locations the uncertainties are smaller than 15 km s^{-1} .

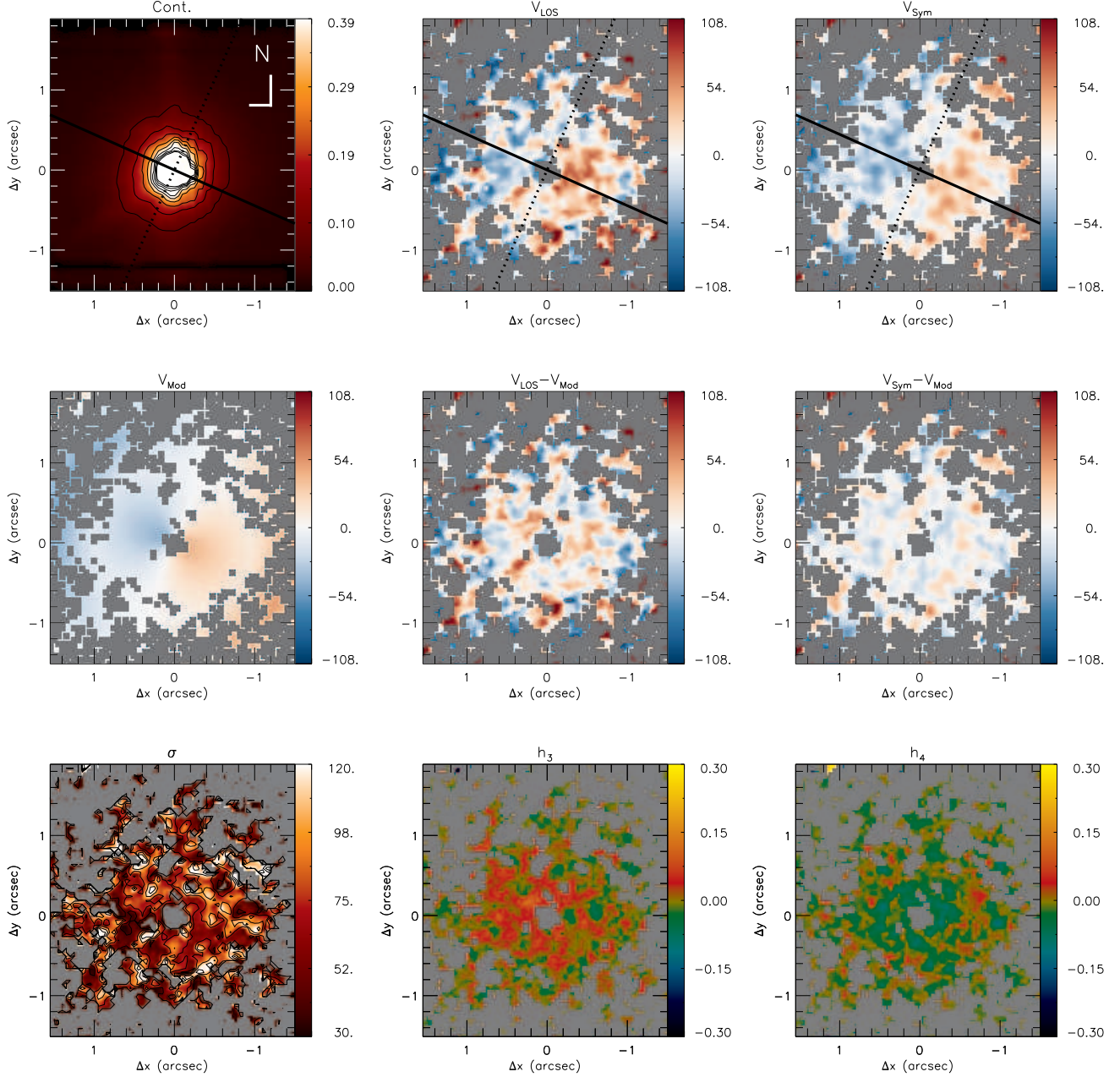


Figure 12. Same as Fig. 2 for Mrk 766.

A rotating disk pattern is recognized in the LOS velocity field for all galaxies, with a straight zero velocity line for most of them. For two galaxies – Mrk 1066 (Riffel & Storchi-Bergmann 2011a) and NGC 5899 (Fig. 10) – an *S* shape zero velocity line is observed, which is a signature of the presence of a nuclear bar or spiral arms in these galaxies (e.g. Combes et al. 1995; Emsellem et al. 2006). For most galaxies, the maximum amplitude of the rotation curve is expected to be observed outside of the NIFS FoV. The rotation disk signature is clearly seen in the one-dimensional plots shown in Fig. B1, obtained by averaging the velocity and σ values within a pseudo-slit with width of $0''.25$ oriented along the major axis of the galaxy. The deprojected velocity amplitude within the NIFS FoV ranges from ~ 50 to ~ 300 km s $^{-1}$.

For 5 galaxies, the maximum σ value is smaller than 100 km s $^{-1}$, 7 have maximum σ in the range 100–150 km s $^{-1}$ and 4 show the maximum $\sigma > 150$ km s $^{-1}$. In addition, distinct structures of low- σ values (~ 50 –80 km s $^{-1}$) are seen in the maps: low- σ rings or partial rings are seen for Mrk 1066, Mrk 1157, NGC 5929 and NGC 788. These rings have been identified by visual inspection and are marked in the corresponding σ maps as green ellipses. In all cases the size of the structures is larger than the spatial resolution and the σ decrease is larger than the velocity resolution of the data. These structures have been attributed to intermediate-age stellar populations (ages in the range 100–700 Myr; e.g. Riffel et al. 2010, 2011), with origin in kinematically colder regions that still preserve the kinematics of the

gas from which they have been formed. Patches of low- σ are seen for Mrk 607, NGC 2110, NGC 3516, NGC 4051, NGC 4235 and NGC 5899, while three objects (NGC 1052, NGC 3227 and NGC 4388) show a centrally peaked σ distribution. These rings and partial rings are located at distances from the nucleus ranging between 150 and 250 pc. Nuclear σ values for each galaxy are presented in the last column of Table 2, obtained by fitting the nuclear spectrum integrated within a circular aperture with radius of 75 pc.

Most galaxies show low h_3 values ($-0.10 < h_3 < 0.10$), suggesting that their LOSVDs are well represented by a Gaussian velocity distribution. Exceptions are Mrk 607, Mrk 1066 and NGC 4051 that show h_3 values larger than 0.15. For 8 galaxies (NGC 1052, NGC 2110, NGC 3227, NGC 3516, NGC 4051, NGC 5506, Mrk 607 and Mrk 1066), the h_3 map is anti-correlated with the velocity field, with positive h_3 values seen at locations where rotation velocities are observed in blueshifts and negative h_3 values associated to regions where the rotation velocities are observed in redshifts. A similar trend (but not so clear) is observed for other four galaxies (NGC 4235, NGC 4388, NGC 5929 and Mrk 1157). In Fig. B2 of the Appendix B we present plots of the LOS velocity vs. h_3 for all galaxies, which show this anti-correlation clearly. The anti-correlation seen between h_3 and the LOS velocity can be interpreted as due to the contribution of stars rotating slower than those in the galaxy disk, probably due to motion in the galaxy bulge (e.g. Emsellem et al. 2006; Ricci, Steiner & Menezes 2016).

The h_4 moment maps show small values at most locations for all galaxies, with $-0.05 < h_4 < 0.05$. For some galaxies, that present strong low- σ structures (e.g., Mrk 1066, Mrk 607 and NGC 4051), higher positive h_4 values are observed co-spatial with the low- σ regions. This is also seen in the plots presented in Fig. B2, that show a trend of higher values of σ being observed in regions with negative h_4 values, while small σ values being associated to positive h_4 values. We interpret this correlation between low- σ and high h_4 values as an additional support to the presence of young/intermediate age stars at these locations, as more peaked velocity distributions are expected for young stars (as they are located in a thin disk structure).

The rotating disk models reproduce well the observed velocity fields for all galaxies, as seen in the residual velocity maps that show values smaller than 20 km s^{-1} at most locations. Table 2 shows the model parameters for each galaxy. The systemic velocities from the table are relative to the heliocentric frame. The de-projected velocity amplitude of the galaxies of our sample ranges from $\sim 60 \text{ km s}^{-1}$ (for NGC 4051 - a Sc galaxy) to $\sim 340 \text{ km s}^{-1}$ (for NGC 3516 - a S0 galaxy).

5 DISCUSSIONS

5.1 Comparison between kinematic and large scale disk parameters

Table 2 shows the parameters derived from the symmetrization (using the FitKinematicPA routine) and from the fit of the rotation disk model (using the DiskFit code) of the velocity fields. These parameters can be compared to those obtained for the large scale disks. The position angle (PA) of the major axis from NED² (Ψ_{ONED}), shown in Table 2 is derived from the K_S band photometry obtained

from the Two Micron All Sky Survey (2MASS, Jarrett et al. 2003). The ellipticity (e_{NED}) and inclination (i_{NED}) of the disk are also obtained from the apparent major (a) and minor (b) axis available on NED database from K_S images, as $e_{\text{NED}} = 1 - \frac{b}{a}$ and $i_{\text{NED}} = \arccos(b/a)$, respectively.

In the left panel of Figure 13 we present a plot of the large scale photometric PA of the major axis *versus* the kinematic PA derived from our NIFS velocity fields, constructed using the values of Ψ_0 shown in Table 2. This plot shows that the small scale kinematic PA is in approximate agreement with the large scale photometric one. The mean PA offset is $\langle \Psi_0 - \Psi_{\text{ONED}} \rangle = 3.9^\circ \pm 5.7^\circ$. Only for three galaxies (NGC 5548, Mrk 766 and NGC 3516) there are significant discrepancies between small scale kinematic and large scale photometric major axes. NGC 5548 and Mrk 766 are almost face on galaxies and thus it is hard to obtain a precise determination of Ψ_0 , both from photometry and kinematics, justifying the discrepancy. For NGC 3516 the Ψ_{ONED} is distinct from that observed in optical images ($\Psi_0 = 56^\circ$, Schmitt & Kinney 2000) and from the stellar kinematics based on optical IFS ($\Psi_0 = 53^\circ$, Arribas et al. 1993). On the other hand, the Ψ_{ONED} for NGC 3516 is very similar to the orientation of the bar of the galaxy ($\Psi_0 = -10^\circ$, Veilleux et al. 1993) and thus the value of Ψ_{ONED} may be biased due to the bar, that is stronger in near-IR bands.

Previous studies have found similar results. For example, the morphological study by Malkan, Gorjian & Tam (1998) of the inner kiloparsecs of nearby active galaxies showed that the resulting classification of the small scale structure was very similar to the one given in the Third Reference Catalog (RC3, Corwin, Buta & de Vaucouleurs 1994), showing that not only the kinematic PA at small scale but also the photometric PA at small scale is similar to that at large scale.

Barbosa et al. (2006) used the Gemini Multi-Object Spectrograph (GMOS) IFU to map the stellar kinematics of the inner 200–900 pc of six nearby active galaxies by fitting the stellar absorption lines of the Calcium triplet around 8500\AA and also found that the kinematic position angle at small scale is in good agreement with the large scale photometric measurements. Dumas et al. (2007) used optical IFS to map the stellar and gas kinematics of the central kiloparsec of a matched sample of nearby Seyfert and inactive galaxies at angular resolutions ranging from $0''.9$ to $2''.5$, using the SAURON IFU on the William Herschel Telescope. They found that the orientations of the kinematic line of nodes are very similar with those derived from large scale photometry for both active and inactive galaxies. Falc3n-Barroso et al. (2006) present the stellar kinematics of a sample of 24 spiral galaxies using the SAURON IFU. Their sample includes only 5 active nuclei and they found misaligned photometric and kinematic axes for 9 objects in their sample (only one being an active galaxy), interpreted as being due to non-axisymmetric structures (as bars) and more easily detected at low galaxy inclinations.

The middle and right panels of Figure 13 show the comparison between the large photometric (y-axis) and small kinematic (x-axis) scale disk inclination and ellipticity, respectively. In contrast to the orientation of the major axis of the galaxy, these parameters do not follow the same distribution at small and large scale. For most cases, both the inclination and the ellipticity of the disk at large scale are larger than that derived for the inner $3'' \times 3''$. This result can be interpreted as being due to the fact that the large scale measurements are dominated by the disk component as they are estimated from the apparent major and minor axis measurements obtained from large scale K_S images, while at small scale, the near-IR emission is dominated by emission from evolved red stars at the

² NASA/IPAC Extragalactic Database available at <http://ned.ipac.caltech.edu/>

Table 2. Kinematic parameters obtained by symmetrize the stellar velocity. Col. 1: Galaxy name; cols 2-3: systemic velocity (V_s) corrected for the heliocentric frame and orientation of the line of nodes (Ψ_0) derived from the symmetrization of the velocity fields; cols 4-5: disk ellipticity (e) and inclination (i) derived by modeling the velocity field using the DiskFit routine; cols 6-8: orientation of the major axis, ellipticity and inclination of the large scale disk, as available at NED; col 9: the nuclear stellar velocity dispersion measured within a circular aperture with 150 pc diameter.

Galaxy	FitKinematicPA		DiskFit		Large Scale Disk			
	V_s (km s $^{-1}$)	$\Psi_0(^{\circ})$	e	$i(^{\circ})$	$\Psi_{0NED}(^{\circ})$	e_{NED}	$i_{NED}(^{\circ})$	σ (km s $^{-1}$)
NGC788	4034	120 \pm 3	0.07 \pm 0.01	20.8 \pm 0.2	100	0.67	42.3	187 \pm 4
NGC1052	1442	114 \pm 3	0.32 \pm 0.01	47.5 \pm 0.2	120	0.71	45.6	245 \pm 4
NGC2110	2335	156 \pm 3	0.26 \pm 0.01	42.5 \pm 0.3	160	0.63	38.7	238 \pm 5
NGC3227	1174	156 \pm 3	0.30 \pm 0.01	45.4 \pm 0.2	152	0.88	62.0	130 \pm 7
NGC3516	2631	54 \pm 3	0.05 \pm 0.01	18.2 \pm 0.8	7	0.69	43.9	186 \pm 3
NGC4051	717	130 \pm 9	0.20 \pm 0.01	37.3 \pm 0.9	142	0.84	56.6	72 \pm 3
NGC4235	2276	54 \pm 3	0.25 \pm 0.01	41.2 \pm 0.5	50	0.94	70.1	183 \pm 12
NGC4388	2537	96 \pm 3	0.11 \pm 0.01	27.7 \pm 0.3	89	0.95	71.3	106 \pm 6
NGC5506	1878	96 \pm 3	0.48 \pm 0.01	58.7 \pm 0.3	90	0.97	76.1	-
NGC5548	5128	108 \pm 3	0.51 \pm 0.04	60.9 \pm 6.8	60	0.34	19.9	276 \pm 22
NGC5899	2616	24 \pm 3	0.54 \pm 0.01	62.7 \pm 0.3	25	0.92	67.7	147 \pm 9
NGC5929	2491	30 \pm 9	0.51 \pm 0.01	60.7 \pm 0.5	38	0.69	43.9	134 \pm 5
MRK607	2781	138 \pm 3	0.47 \pm 0.01	58.2 \pm 0.1	135	0.94	70.1	132 \pm 4
MRK766	3855	66 \pm 3	0.05 \pm 0.02	18.2 \pm 3.7	110	0.77	50.2	78 \pm 6
MRK1066	3583	120 \pm 3	0.36 \pm 0.01	50.2 \pm 0.3	140	0.92	66.4	103 \pm 4
MRK1157	4483	114 \pm 3	0.29 \pm 0.01	45.1 \pm 0.9	95	0.88	61.3	92 \pm 4

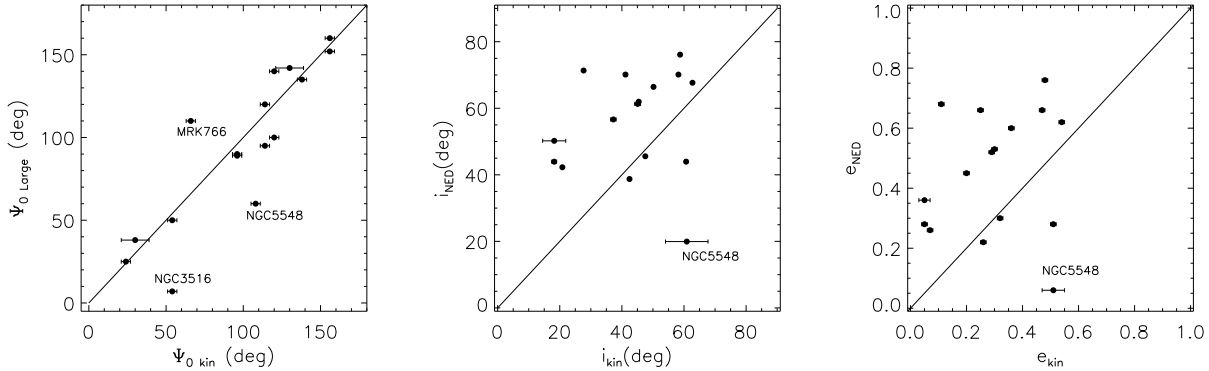


Figure 13. Comparison of large scale photometric (y-axis) and small scale kinematic (x-axis) PAs (left), inclination (middle) and ellipticity (right). Continuous lines show one-to-one relations.

bulge of the galaxy (e.g. Maraston 2005; Riffel et al. 2015c), which play an important role in the observed morphology and kinematics observed with NIFS.

5.2 Gravitational potentials and comparison with previous studies

The velocity residual maps for all galaxies of our sample show small values, indicating that the stellar velocity fields are well reproduced by the rotating disk model, with kinematic axes that follows the same orientation of large scale measurements. In addition, the deprojected rotation velocity amplitude is always larger than the mean velocity dispersion, indicating the the stellar kinematics of the galaxies of our sample are dominated by regular rotation. We can compare our results with previous studies of the stellar kinematics of active and inactive galaxies.

Dumas et al. (2007) present the stellar kinematics of a sample of 39 active galaxies and a matched control sample, selected to

have similar blue magnitudes, Hubble type and inclinations. They found that the stellar kinematics of both active and inactive galaxies show regular rotation patterns typical of disc-like systems. A similar result was found by Barbosa et al. (2006) using higher angular resolution ($<1''.0$) IFS with Gemini Telescopes of a sample of six nearby Seyfert galaxies. In addition, they found partial rings of low- σ values at 200–400 pc from the nucleus for three galaxies, interpreted as tracers of recently formed stars that partially keep the cold kinematics of the original gas from which they have formed. Falc3n-Barroso et al. (2006) present kinematic maps for a sample of nearby spiral galaxies obtained with the SAURON IFU, which show regular stellar rotation for most galaxies. However, kinematic decoupled components are frequently seen in the inner region, as sudden changes in the velocity field, which are often associated with a drop in the σ and anti-correlated h_3 values with respect to the V_{Los} . In addition, they found kinematic signatures of non-axisymmetric structures for 37% of the galaxies of their sample (only one harboring an AGN). For 20 % of their sample (5 galaxies,

none of them harboring an AGN) they found kinematic signatures of bars as predicted in N-body simulations of barred potentials (e.g. Kuijken & Merrifield 1995; Bureau & Athanassoula 2005).

Hubble Space Telescope (HST) H-band images up to $10''$ radius and ground-based near-infrared and optical images of a matched Seyfert versus non-Seyfert galaxy sample of 112 nearby galaxies show a statistically significant excess of bars among the Seyfert galaxies at practically all length-scales (Laine et al. 2002). In addition, they also found that Seyfert galaxies always show a preponderance of “thick” bars compared to the bars in non-Seyfert galaxies. On the other hand, recent results show that AGN hosts at $0.2 < z < 1.0$ show no statistically significant enhancement in bar fraction compared to inactive galaxies (e.g. Cheung et al. 2015). Large scale bars are seen for 28.5% of face-on spiral hosts of AGN, as obtained from the study of more the 6.000 AGN hosts of from the Sloan Digital Sky Survey (SDSS; Alonso, Coldwell & Lambas 2013).

Our kinematic maps suggest the presence of nuclear bars in only 2 galaxies: Mrk 1066 and NGC 5899, as revealed by the presence of an S shape zero velocity line observed in the V_{LOS} maps (e.g. Combes et al. 1995; Emsellem et al. 2006). This corresponds to only 12.5% of our sample, although the statistics is low so far and this result is preliminary. The rest of the galaxies are dominated by rotation. The difference in the proportion of barred galaxies or non-axisymmetric structures in our study relative to that of Falcón-Barroso et al. (2006) may be due to the small number of objects in both studies, and to the difference in the field-of-view (FoV) of the two studies. Our FoV ($3'' \times 3''$) is smaller than those of previous studies, making it more difficult to identify kinematic signatures of bars as predicted in N-body simulations (e.g. Bureau & Athanassoula 2005), as double-hump rotation curves, broad σ profiles with a plateau at moderate radii and $h_3 - V_{LOS}$ correlation over the projected bar length. On the other hand, the photometric detection of bars mentioned above are mainly obtained using large scale images. Thus, our results suggest that the motion of the stars is dominated by the gravitational potential of the bulge, as the FoV of our observations is smaller than the bulge length for all galaxies.

In order to further investigate how the galactic potentials and deviations from ordered rotation are related to the host galaxy and AGN, we plotted the mean value of the modulus of the residual velocities ($\langle |V_{res}| \rangle$), where $V_{res} = V_{LOS} - V_{mod}$, against the Hubble index and hard X-ray (14–195 keV) luminosity (L_X) from the Swift-BAT 60-month catalogue (Ajello et al. 2012), which measures direct emission from the AGN. These plots are shown in Figure 14. For four galaxies of our sample (MRK1066, MRK1157, MRK607 and NGC5929), there are no X-ray luminosities available in the BAT catalogue and thus the $\langle |V_{res}| \rangle$ vs. plot contains only 12 points. The $\langle |V_{res}| \rangle$ was estimated as the mean value of 10.000 bootstrap realizations in which for each interaction the $|V_{res}|$ is calculated for a sample selected randomly among the values observed in the residual map. The standard deviation in the simulated $|V_{res}|$ represents the intrinsic scatter of each residual map and is used as the uncertainty for $\langle |V_{res}| \rangle$.

The top panel of Fig. 14 shows that there is no correlation between $\langle |V_{res}| \rangle$ and Hubble index, with a Pearson correlation coefficient of only $R = 0.12$. This result shows that large scale structures do not affect significantly the stellar kinematics of the inner kiloparsec of the galaxies of our sample.

On the other hand, the bottom panel of Fig. 14 suggests that $\langle |V_{res}| \rangle$ is correlated with L_X . We computed a Pearson correlation coefficient of $R = 0.74$, with less than 1 % of probability that

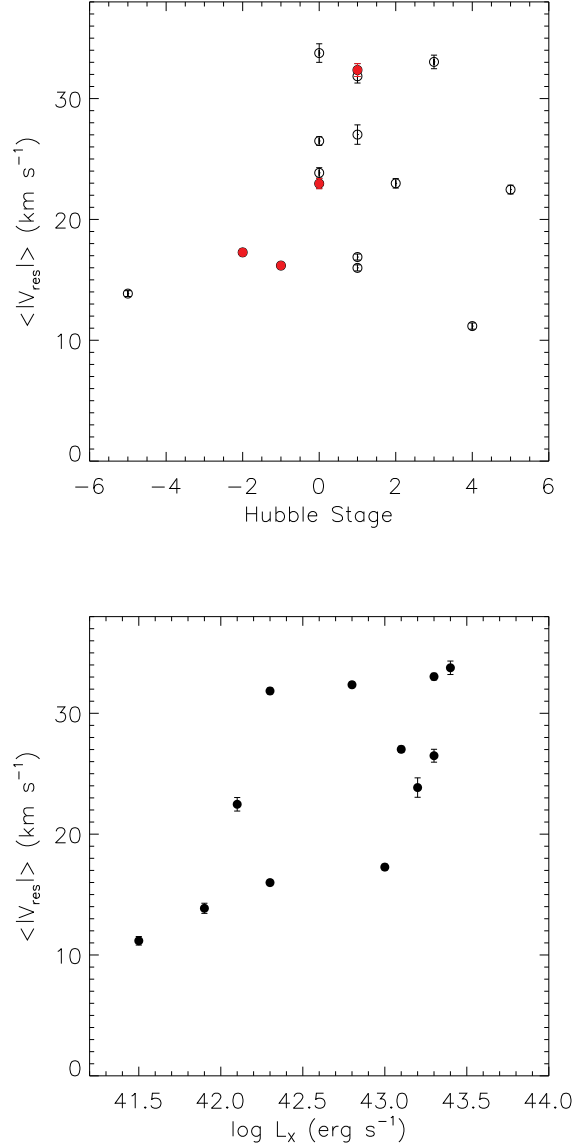


Figure 14. Plots of the standard deviation of the residual maps ($\langle |V_{res}| \rangle$) vs. Hubble index (top) and X-ray luminosity (L_X , bottom). In the top panel, filled circles correspond to barred galaxies.

this distribution of points can be generated by a random distribution. Although the number of points is small, this trend may mean that more luminous AGN have a larger impact in the surrounding stellar dynamics. As a speculation, we propose that strong AGN may quench circum-nuclear star formation in the galaxy disk and thus the stellar motions have a more important component of bulge star kinematics. On the other hand, for lower luminosity AGNs, the active nuclei may not be powerful enough to quench the star formation and thus the stellar dynamics has a stronger contribution from stars more recently formed in the plane of the galaxy.

5.3 Implications to AGN feeding and star formation

The velocity dispersion maps show structures of lower σ than the surroundings (~ 50 – 80 km s⁻¹) for 10 galaxies (62 %)

of our sample. Such velocity dispersion drops are commonly reported in the literature (e.g. Bottema 1989, 1993; Fisher 1997; García-Lorenzo, Mediavilla & Arribas 1999; Emsellem et al. 2001; Márquez et al. 2003; Falcón-Barroso et al. 2006; Barbosa et al. 2006) and have been interpreted as being tracers of relatively recent star formation as compared to the bulge stellar population (e.g. Emsellem et al. 2001, 2006; Márquez et al. 2003; Barbosa et al. 2006; Riffel et al. 2008). Indeed, stellar population synthesis using near-IR IFS with NIFS reveal that the low- σ rings seen in Mrk1066 and Mrk1157 are associated to an intermediate-age stellar population (<700 Myr; Riffel et al. 2010, 2011).

The low- σ structures may be related to accretion of gas to the inner kiloparsec of galaxies as a result of streaming motions towards the nucleus along nuclear bars or dust spirals, observed for several active galaxies by our group (e.g. Fathi et al. 2006; Riffel et al. 2008; Storchi-Bergmann et al. 2009; Riffel et al. 2013; Diniz et al. 2015; Schnorr-Müller et al. 2014, 2016, 2017; Lena et al. 2015) and other groups (e.g. van de Ven & Fathi 2009; Sánchez et al. 2009; Smajić et al. 2015). Several works have been aimed to investigate the presence of nuclear bars and dust spirals in active and inactive galaxies using high resolution HST images (Laine et al. 2002; Pogge & Martini 2002; Simões Lopes et al. 2007; Martini, Dicken & Storchi-Bergmann 2013). These studies reveal an excess of bars in Seyfert galaxies, when compared to a matched sample of inactive galaxies (Laine et al. 2002) and dust structures seem to be present in all early type AGN hosts, while only 26 % of inactive early type show significant dust in the nuclear region (Simões Lopes et al. 2007). For late type galaxies, large amount of dust is observed for both active and inactive galaxies (Simões Lopes et al. 2007).

The observed gas inflows mentioned above can lead to the accumulation of large reservoirs of gas that can feed both star formation and the AGN. In such scenario, it would be expected that low- σ structures should be more frequent in active than in inactive galaxies. However, several studies report the presence of low- σ structures in inactive galaxies. For example, Falcón-Barroso et al. (2006) found that at least 46 % of their sample of spiral galaxies show σ -drops, most of them being inactive. A similar result is reported by Ganda et al. (2006), who found central σ drops for many objects of their sample of 18 spiral galaxies. On the other hand, these drops are not commonly observed in elliptical galaxies (Emsellem et al. 2004). Thus, the presence of low- σ may be related to recent star formation in the inner kiloparsec of the galaxies of our sample, but possibly unrelated to the nuclear activity.

5.4 The stellar kinematics and AGN Feeding and Feedback processes

This paper is the first of a series in which we will investigate the AGN feeding and feedback processes using J and K band NIFS observations of a sample of nearby active galaxies selected using as main criteria the hard X-ray luminosity. The results presented here will be used to compare gas and stellar kinematics in order to isolate non-circular motions, by constructing residual maps between the observed velocity fields for the ionized (traced by [Fe II] and H recombination lines) and molecular (traced by H₂ emission lines) gas and the rotating disk models presented here. The analysis of the residual maps, together with velocity channel maps along the emission-line profiles, will allow us to identify possible gas inflows and outflows. Similar methodology has already been successfully used by our AGNIFS group (e.g.

Riffel et al. 2008; Riffel & Storchi-Bergmann 2011a; Riffel et al. 2013; Riffel & Storchi-Bergmann 2011b; Diniz et al. 2015). The gas inflow and outflow rates can be compared with AGN properties (e.g. bolometric luminosity and accretion rate) to draw a picture of the feeding and feedback processes in AGNs.

6 CONCLUSIONS

We used near-IR integral field spectroscopy to map the stellar kinematics of the inner $3'' \times 3''$ of a sample of 16 nearby Seyfert galaxies. We present maps for the radial velocity, velocity dispersion and higher order Gauss Hermite moments, obtained by fitting the CO stellar absorptions in the K-band. The observed velocity fields were symmetrized and modeled by a thin rotating disk in order to derive kinematical parameters. The main results of this work are:

- The observed velocity fields for all galaxies show regular rotation. In addition, for two galaxies (Mrk 1066 and NGC 5899) the velocity field shows an S shape zero velocity line which is interpreted as a signature of nuclear bars.
- The residuals of the modeling of the stellar velocity field are correlated with the hard X-ray luminosity, suggesting that the nuclear source plays a role on the observed stellar dynamics of the inner kiloparsec of the galaxies, with stronger AGNs showing less ordered stellar orbits than weak AGNs.
- The velocity dispersion maps show low- σ ($\sim 50 - 80 \text{ km s}^{-1}$) rings for 4 galaxies (Mrk 1066, Mrk 1157, NGC 5929 and NGC 788) or “patches” of low- σ structures (for Mrk 607, NGC 2110, NGC 3516, NGC 4051, NGC 4235 and NGC 5899) at typical distances of 200 pc, interpreted as being originated in young/intermediate age stellar populations. Centrally peaked σ maps are observed for three galaxies (NGC 1052, NGC 3227 and NGC 4388).
- The h_3 moment is anti-correlated with the velocity field for 8 galaxies (NGC 1052, NGC 2110, NGC 3227, NGC 3516, NGC 4051, NGC 5506, Mrk 607 and Mrk 1066) – positive h_3 values seen at locations where the velocity field shows blueshifts and $h_3 < 0$ for locations where the velocity field shows redshifts. The presence of these wings are attributed to the contribution of stars from the galaxy bulge that present lower rotation velocities.
- The h_4 maps show small values at most locations for all galaxies. For the galaxies with low- σ rings, higher h_4 values are observed co-spatially with the ring, being interpreted as an additional signature of young/intermediate age stars at these locations.
- The observed velocity fields are well reproduced by a rotating disk model, with deprojected velocity amplitudes in the range $\sim 60 - 340 \text{ km s}^{-1}$.
- The orientations of the line of nodes derived from the small scale velocity fields are similar to the photometric major axis orientations of the large scale disks, while the disk ellipticity and inclination are smaller at small scale, as compared to those at large scale.

The stellar kinematics and rotating disk models derived in this work will be compared to the gas kinematics and flux distributions in future studies with the aim of isolating and quantifying non-circular motions in the gas of the galaxies of our sample in order to map and quantify feeding and feedback processes in our AGN sample.

ACKNOWLEDGMENTS

We thank an anonymous referee for useful suggestions which helped to improve the paper. Based on observations obtained at the Gemini Observatory, which is operated by the Association of Universities for Research in Astronomy, Inc., under a cooperative agreement with the NSF on behalf of the Gemini partnership: the National Science Foundation (United States), the Science and Technology Facilities Council (United Kingdom), the National Research Council (Canada), CONICYT (Chile), the Australian Research Council (Australia), Ministério da Ciência e Tecnologia (Brazil) and south-east CYT (Argentina).

This research has made use of the NASA/IPAC Extragalactic Database (NED) which is operated by the Jet Propulsion Laboratory, California Institute of Technology, under contract with the National Aeronautics and Space Administration. We acknowledge the usage of the HyperLeda database (<http://leda.univ-lyon1.fr>). *R.A.R.* and *R. R.* thank to CNPq and FAPERGS for financial support.

REFERENCES

- Ajello, M., Alexander, D. M., Greiner, J., Madejski, G. M., Gehrels, N., Burlon, D., 2012, *ApJ*, 749, 21.
- Alonso, M. S., Coldwell, G., Lambas, D. G., 2013, *A&A*, 549, A141.
- Arribas, S., Mediavilla, E., García-Lorenzo, B., Del Burgo, C., 1997, *ApJ*, 490, 227.
- Barbosa, F. K. B., Storch-Bergmann, T., Cid Fernandes, R., Winge, C., & Schmitt, H. 2006, *MNRAS*, 371, 170.
- Barbosa, F. K. B., Storch-Bergmann, T., Cid Fernandes, R., Winge, C., Schmitt, H., 2009, *MNRAS*, 396, 2.
- Barbosa, F. K., Storch-Bergmann, McGregor, P., Vale, T. B., Riffel, R. A., 2014, *MNRAS*, 455, 2353.
- Barnes, E. I., Sellwood, J. A., 2003, *AJ*, 125, 1164.
- Bottema R., 1989, *A&A*, 221, 236
- Bottema R., 1993, *A&A*, 275, 16.
- Bureau M., Athanassoula E., 2005, *ApJ*, 626, 159
- Cappellari & Emsellem, 2004, *PASP*, 116, 138.
- Cappellari, M. et al., 2007, *MNRAS*, 379, 418.
- Cheung, E. et al., 2015, *MNRAS*, 447, 506.
- Ciotti, L., et al. 2010, *ApJ* 717, 707
- Combes, F., Boissé, P., Mazure, A. & Blanchard, A., 1995, *Galaxies and Cosmology*, Springer-Verlag, Berlin, Germany.
- Corwin, H.G., Buta, R.J., de Vaucouleurs, G. 1994, *AJ*, 108, 2128
- Davies, R. I., Thomas, J., Genzel, R., Mueller Sánchez, F., Tacconi, L. J., Sternberg, A., Eisenhauer, F., Abuter, R., Saglia, R., & Bender, R., 2006, *AJ*, 646, 754.
- Diniz, M. R., Riffel, R. A., Storch-Bergmann, T., Winge, C., 2015, *MNRAS*, 453, 1727.
- Dumas, G., Mundell, C. G., Emsellem, E., & Nagar, N. M. 2007, *MNRAS*, 379, 1249.
- Emsellem E., Greusard D., Combes F., Friedli D., Leon S., Pécontal E., Wozniak H., 2001, *A&A*, 368, 52
- Emsellem E. et al., 2004, *MNRAS*, 352, 721
- Emsellem, E., Fathi, K., Wozniak, H., Ferruit, P., Mundell, C. G., Schinnerer, E. 2006, *MNRAS*, 365, 367.
- Elvis, M. 2000, *ApJ*, 545, 63
- Fabian, A. 2012, *ARA&A*, 50, 455
- Falcón-Barroso, J. et al., 2006, *MNRAS*, 369, 529.
- Fathi, K., Storch-Bergmann, T., Riffel, R. A., Winge, C., Axon, D. J., Robinson, A., Capetti, A., & Marconi, A., 2006, *ApJ*, 641, L25.
- Ferrarese, L. & Ford, H. 2005, *SSRv*, 116, 523
- Fisher D., 1997, *AJ*, 113, 950
- Fischer, T. C., Crenshaw, D. M., Kraemer, S. B., Schmitt, H. R., Storch-Bergmann, T., Riffel, R. A., 2015, *ApJ*, 799, 234.
- Frank, J., King, A. & Raine, D. J., 2002, *Accretion Power in Astrophysics*, Cambridge Univ. Press
- Ganda, K., Falcón-Barroso, J., Peletier, R. F., Cappellari, M., Emsellem, E., McDermid, R. M., de Zeeuw, P. T., Carollo, C. M., 2006, *MNRAS*, 367, 46.
- García-Lorenzo B., Mediavilla E., Arribas S., 1999, *ApJ*, 518, 190
- Gerhard, O. E., 1993, *MNRAS*, 265, 213.
- Hicks, E. K. S., Davies, R. I., Malkan, M. A., Genzel, R., Tacconi, L. J., Sánchez, F. M., Sternberg, A., 2009, *ApJ*, 696, 448.
- Hicks, E. et al. 2013, *ApJ*, 768, 107
- Jarrett, T. H.; Chester, T.; Cutri, R.; Schneider, S. E.; Huchra, J. P., 2003, *AJ*, 125, 525.
- Kormendy, J. & Ho, L. C. 2013, *ARA&A*, 51, 511
- Krajnović, D., Cappellari, M., de Zeeuw, P. T., Copin, Y., 2006, *MNRAS*, 366, 787.
- Krajnović, D. et al., 2011, *MNRAS*, 414, 2993.
- Kuijken K., Merrifield M. R., 1995, *ApJ*, 443, L13
- Kuzio de Naray, R., Arsenault, C. A., Spekkens, K., Sellwood, J. A., McDonald, M., Simon, J. D., Teuben, P., 2012, *MNRAS*, 427, 2523.
- Laine, S., Shlosman, I., Knapen, J. H., Peletier, R. F., 2002, *ApJ*, 567, 97.
- Lena, D., Robinson, A., Storch-Bergman, T., Schnorr-Müller, A., Seelig, T., Riffel, R. A., Nagar, N. M., Couto, G. S., Shadler, L., 2015, *ApJ*, 806, 84.
- Malkan, M. A.; Gorjian, V.; Tam, R., 1998, *ApJS*, 117, 25.
- Maraston, C., 2005, *MNRAS*, 362, 799.
- Márquez I., Masegosa J., Durret F., González Delgado R. M., Moles M., Maza J., Prez E., Roth M., 2003, *A&A*, 409, 459
- Martini, P., Dicken, D., Storch-Bergmann, T., 2013, *MNRAS*, 420, 2249
- Mazzalay, X. et al. 2014, *MNRAS*, 438, 2036
- McGregor, P. J. et al., 2003, *Proceedings of the SPIE*, 4841, 1581.
- Moriondo, G.; Baffa, C.; Casertano, S.; Chincarini, G.; Gavazzi, G.; Giovanardi, C.; Hunt, L. K.; Pierini, D.; Sperandio, M.; Trinchieri, G., 1999, *A&AS*, 137, 101.
- Onken, C. et al., 2014, *ApJ*, 791, 37.
- Pogge R. W., Martini P., 2002, *ApJ*, 569, 624
- Reese, A. S., Williams, T. B., Sellwood, J. A., Barnes, E. I., Powell, B. A., 2007, *AJ*, 133, 2846.
- Ricci, T. V., Steiner, J. E., Menezes, R. B., 2016, *MNRAS*, 463, 3860.
- Riffel, R. A., Storch-Bergmann, T., Winge, C., McGregor, P. J., Beck, T., Schmitt, H., 2008, *MNRAS*, 385, 1129.
- Riffel, R. A., Storch-Bergmann, T., Nagar, N. M., 2010, *MNRAS*, 404, 166.
- Riffel, Rogemar A., 2010, *Ap&SS*, 327, 239.
- Riffel, Rogemar A. & Storch-Bergmann, T., Riffel, R., & Pastoriza, M. G., 2010, *ApJ*, 713, 469.
- Riffel, R. A., Storch-Bergmann, T., 2011, *MNRAS*, 411, 469.
- Riffel, R. A., Storch-Bergmann, T., 2011, *MNRAS*, 417, 2752.
- Riffel et al. 2013, *MNRAS*, 430, 2249
- Riffel, R. A., Storch-Bergmann, T., & Riffel, R., *ApJL*, 2014, 780, 24.
- Riffel, R. A., Storch-Bergmann, T., Riffel, R., 2015, *MNRAS*, 451, 358.
- Riffel, R. A. et al. 2015, *MNRAS*, 446, 2823.
- Riffel, R. et al. 2015, *MNRAS*, 450, 3069.

- Riffel, R., Rodríguez-Ardila, A., Pastoriza, M. G., 2006, *A&A*, 457, 61.
- Riffel, R., Riffel, Rogemar A., Ferrari, F., & Storchi-Bergmann, T., 2011, *MNRAS*, 416, 493.
- Schnorr-Müller, A., Storchi-Bergmann, T., Ferrari, F., Nagar, N. M., 2017, *MNRAS*, 466, 4370
- Schnorr-Müller, A., Storchi-Bergmann, T., Robinson, A., Lena, D., Nagar, N. M., 2016, *MNRAS*, 457, 972
- Schnorr-Müller, A., Storchi-Bergmann, T., Nagar, N. M., Robinson, A., Lena, D., Riffel, R. A., Couto, G. S., 2014, *MNRAS*, 437, 1708.
- Schönell, A. J., Riffel, R. A., Storchi-Bergmann, T., Winge, C., 2014, *MNRAS*, 445, 414.
- Schmitt, H. R., & Kinney, A. L., 2000, *ApJS*, 128, 479.
- Sellwood, J. A., Spekkens, K., 2015, *arXiv:1509.07120*
- Sellwood, J. A., Sánchez, R. Z., 2010, *MNRAS*, 404, 1733.
- Simoes Lopes, R. et al. 2007, *ApJ*, 655, 718
- Spekkens, K., Sellwood, J. A., 2007, *ApJ*, 664, 204.
- Sánchez, F. M., Davies, R. I., Genzel, R., Tacconi, L. J., Eisenhauer, F., Hicks, E. K. S., Friedrich, S., & Sternberg, A., 2009, *ApJ*, 691, 749.
- Somerville et al. 2008, *MNRAS*, 391, 481
- Smajić, S. Moser, L., Eckart, A., Busch, G., Combes, F., García-Burillo, S., Valencia-S., M., Horrobin, M., 2015, *A&A*, 583, A104.
- Springel et al. 2005, *MNRAS*, 361, 776
- Storchi-Bergmann, T., Dors Jr., O., Riffel, R. A., Fathi, K., Axon, D. J., & Robinson, A., 2007, *ApJ*, 670, 959.
- Storchi-Bergmann, T., McGregor, P. Riffel, Rogemar A., Simões Lopes, R., Beck, T., Dopita, M., 2009, *MNRAS*, 394, 1148.
- Storchi-Bergmann, T., Simões Lopes, R., McGregor, P. Riffel, Rogemar A., Beck, T., Martini, P., 2010, *MNRAS*, 402, 819.
- Storchi-Bergmann, T., Riffel, R. A., Riffel, R., Diniz, M., Borges Vale, T., McGregor, P., 2012, *ApJ*, 755, 87.
- Terrazas, B. A., Bell, E. F., Henriques, B. M. B., White, S. D. M., Cattaneo, A., Woo, J., 2016, *ApJL*, 830, L12.
- van der Marel, R.P. & Franx, M. 1993, *ApJ*, 407, 525
- van de Ven, G., & Fathi, K., 2009, *arXiv:0905.3556v1*
- Veilleux, S., Tully, R. B., Bland-Hawthorn, J. 1993, *AJ*, 105, 1318
- Winge, C., Riffel, Rogemar A., Storchi-Bergmann, T., 2009, *ApJS*, 185, 186.

APPENDIX A: STELLAR KINEMATICS BASED ON ALREADY PUBLISHED DATA

Figures A1 – A5 show maps for the stellar kinematics of galaxies with previous measurements already published by our group.

APPENDIX B: ONE-DIMENSIONAL CUTS FOR THE STELLAR KINEMATICS

Figure B1 shows one-dimensional cuts along the major axis of the galaxies for the LOS velocity (left) and σ (right). Plots of the LOS velocity (V_{LOS}) vs. h_3 and σ vs. h_4 using all spaxels are shown in Figure B2.

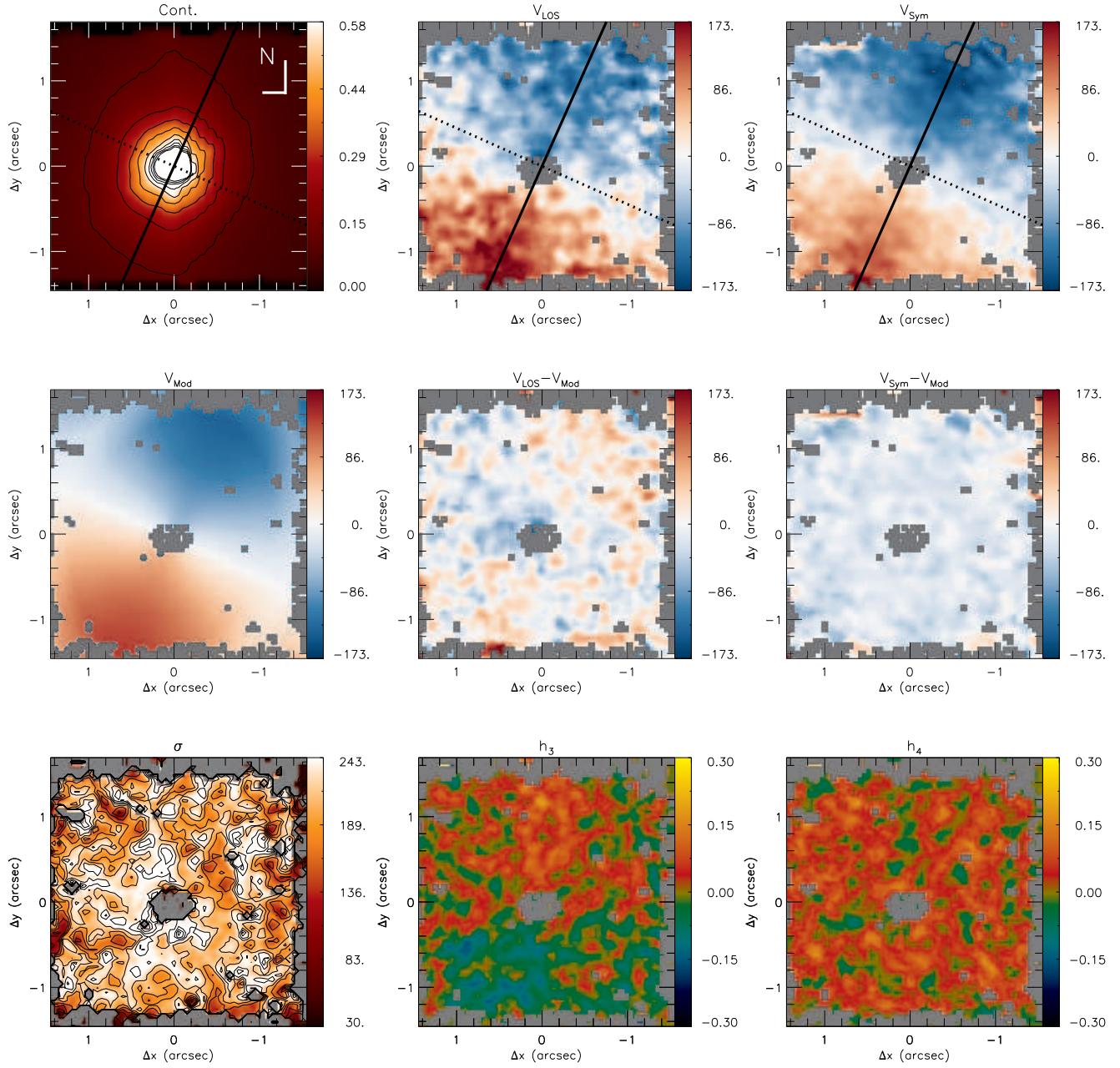


Figure A1. Same as Fig. 2 for NGC 2110. The original stellar kinematics measurements are presented in Diniz et al. (2015)

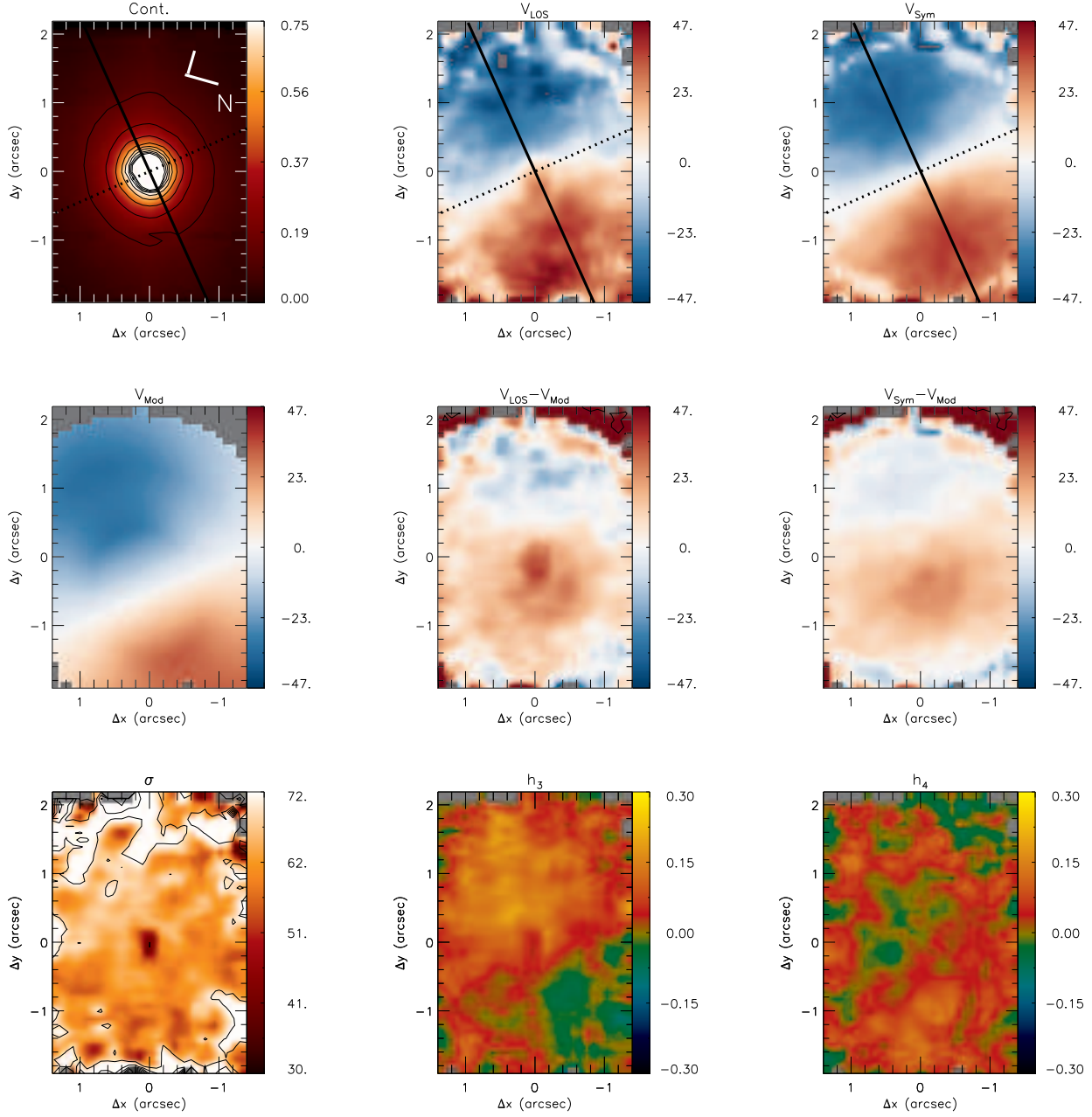


Figure A2. Same as Fig. 2 for NGC 4051. The original stellar kinematics measurements are presented in Riffel et al. (2008)

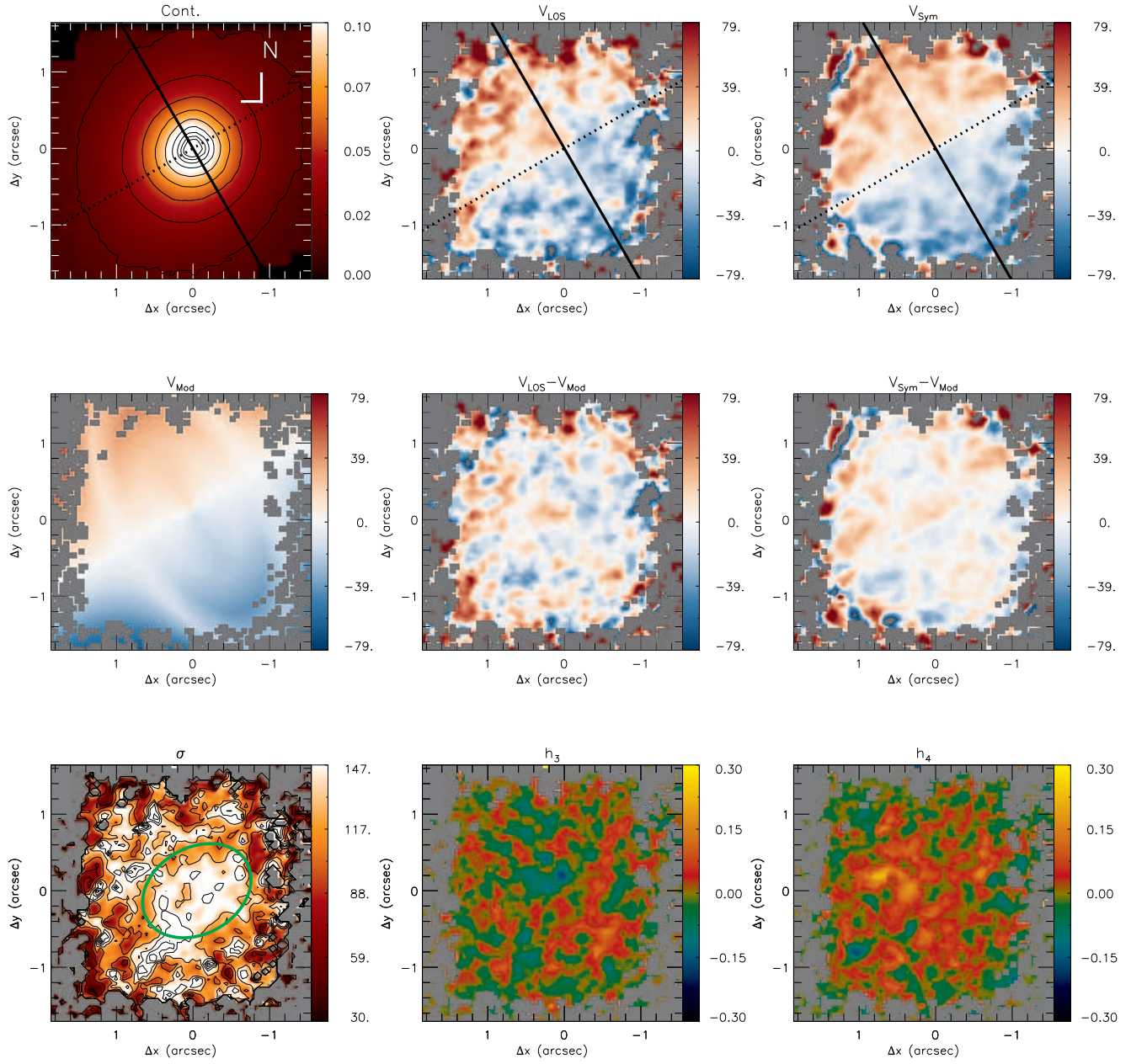


Figure A3. Same as Fig. 2 for NGC 5929. The original stellar kinematics measurements are presented in Riffel et al. (2015a)

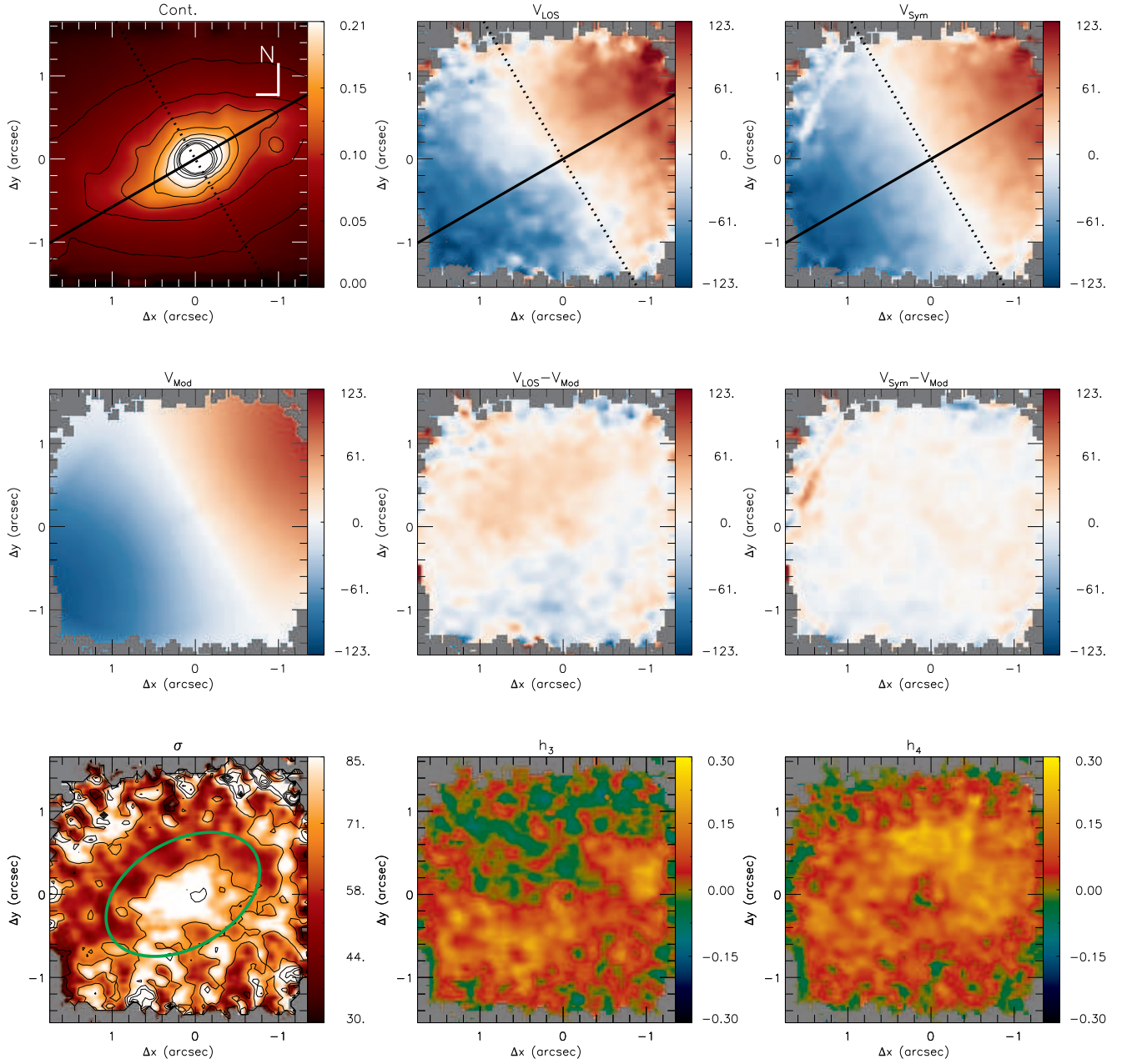


Figure A4. Same as Fig. 2 for Mrk 1066. The original stellar kinematics measurements are presented in Riffel & Storchi-Bergmann (2011a)

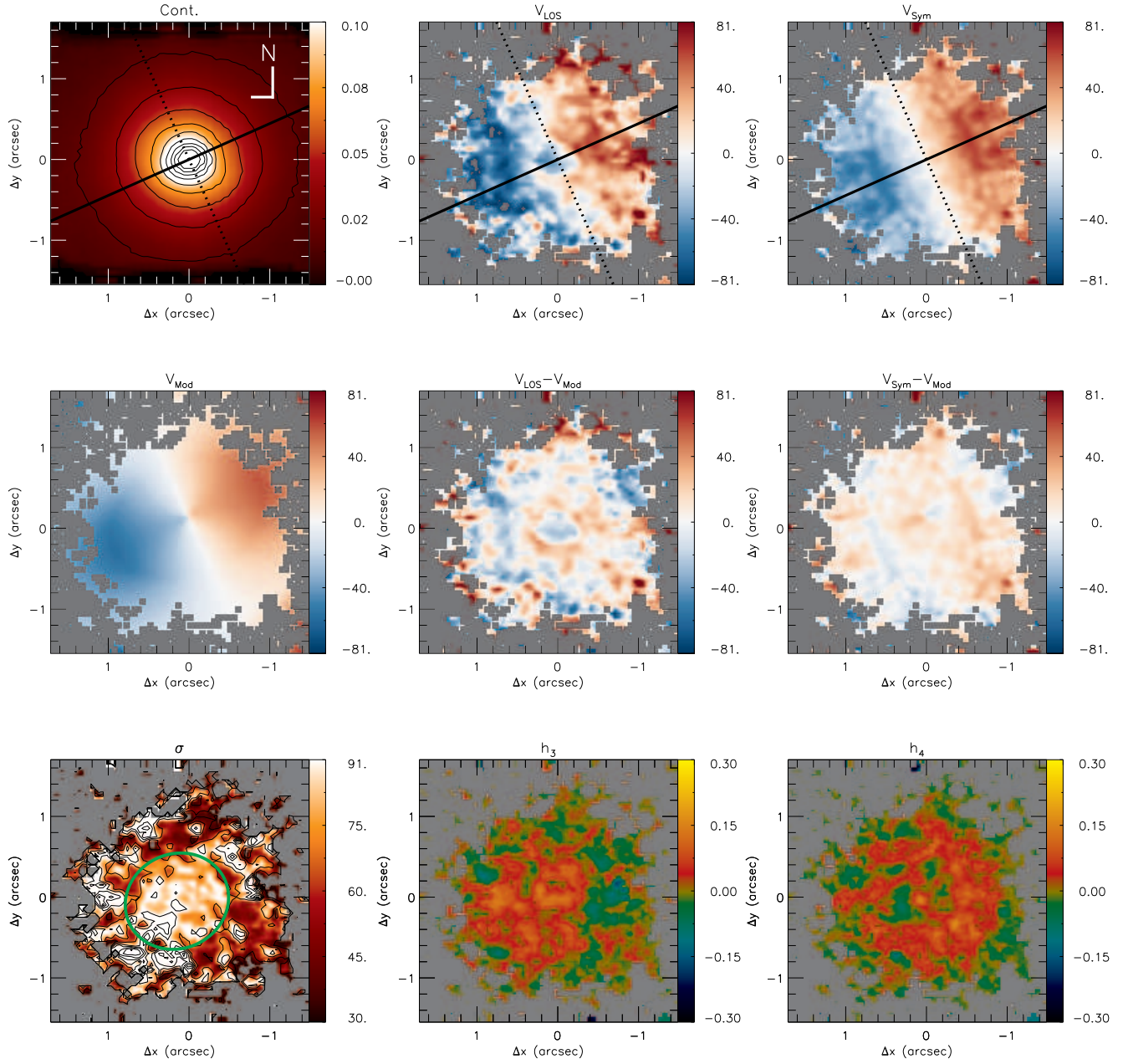


Figure A5. Same as Fig. 2 for Mrk 1157. The original stellar kinematics measurements are presented in Riffel & Storchi-Bergmann (2011b)

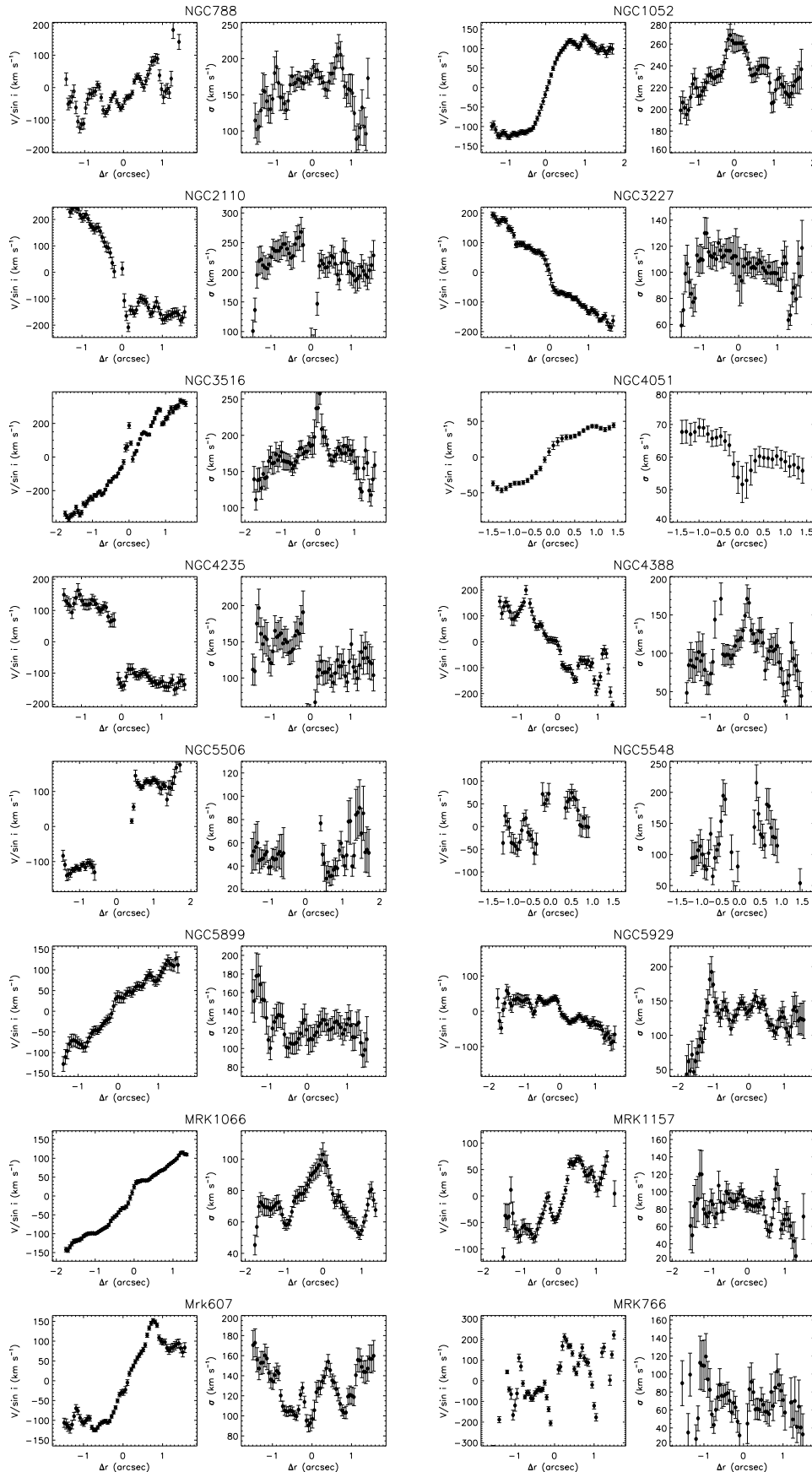


Figure B1. One-dimensional cuts along the major axis of the galaxies obtained by averaging the observed velocities within a pseudo-slit with $0''.25$ width. The orientation of the major axis and the inclination of the disk used in these plots are from Table.2.

